Laser-induced modification of transparent crystals and glasses

N.M. Bulgakova, R. Stoian, A. Rosenfeld

Abstract. **We analyse the processes taking place in transparent crystals and glasses irradiated by ultrashort laser pulses in the regimes typical of various applications in optoelectronics and photonics. We consider some phenomena, which have been previously described by the authors within the different model representations: charging of the dielectric surface due to electron photoemission resulting in a Coulomb explosion; crater shaping by using an adaptive control of the laser pulse shape; optimisation of the waveguide writing in materials strongly resistant to laser-induced compaction under ordinary irradiation conditions. The developed models and analysis of the processes relying on these models include the elements of the solid-state physics, plasma physics, thermodynamics, theory of elasticity and plasticity. Some important experimental observations which require explanations and adequate description are summarised.**

1. Introduction

Laser irradiation of transparent crystalline and amorphous materials is a powerful tool for modifying the properties of the irradiated material [1, 2], the use of which leads to the formation of surface [3–8] and bulk [9–13] periodic structures (nanogratings), to the densification and refractive index change followed by the formation of waveguide structures [14–19], to the formation of microvoids [10, 20–23], to phase transitions (crystallisation or, vice versa, amorphisation) [21, 24], etc. Such modifications are already used in some applications in optoelectronics, photonics (optical signal transmission and optical beam manipulation, 3D writing of information) [25], and microfl-

N.M. Bulgakova S.S. Kutateladze Institute of Thermophysics, Siberian Branch, Russian Academy of Sciences, prosp. akad. Lavrent'eva 1, 630090 Novosibirsk, Russia; e-mail: nbul@itp.nsc.ru;
R. Stoian Laboratoire Hubert Curien, UMR 5516 CNRS, Universite Jean Monnet, 42000 Saint Etienne, Universite de Lyon, 42023 Saint Etienne, France;
A. Rosenfeld Max-Born-Institut für Nichtlineare Optik und Kurzzeitspektroskopie, Max-Born-Strasse 2a, D-12489 Berlin, Germany

uidics [26]; the list of potential applications is rapidly expanding. Successful development of the fields of research and applications based on laser-induced micro- and nano-modifications of transparent crystals and glasses requires understanding of the intricate processes initiated in dielectrics by laser radiation, the processes resulting in formation of permanent mechanically deformed and/or chemically modified states.

Studying theoretically the laser-induced modification of transparent materials is laborious because a chain of different processes initiated by radiation absorption at femtosecond durations extends up to millisecond time scales when the final state of the material becomes 'frozen' in the dielectric matrix. At laser-pulse durations these processes include material photoionisation, avalanche development accompanied by a change in the optical response of the irradiated region of the sample, self-focusing of the laser beam (when the threshold power is reached), and radiation scattering from the produced plasma. Already at subpicosecond durations, active recombination of this 'solid' plasma starts, accompanied by the formation of numerous defect states, thus leading to rapid heating of the photoexcitation region. Nevertheless, maximal heating is achieved at times from several picoseconds to tens of picoseconds. Rapid heating at these time scales is accompanied by generation of thermoelastic waves which, depending on the heating level and heat localisation, can either completely dissipate, or lead to significant plastic deformations of the material, or even to mechanical damages in the form of micro- or nanovoids in the energy-release region. We can conventionally assume that the effects of the mechanical response of the material on photoexcitation terminate by ~ 10 ns, when the three-dimensional elastic compaction wave propagates a distance of a few tens of micrometers and markedly dissipates. However, under some experimental conditions the continuation of the 'mechanical scenario' is possible at time scales of tens of microseconds, when the locally released energy spreads due to heat conduction effects and reaches the 'cold' deformation regions. Melting (softening) of the deformed region results in stress unloading waves which can lead to a significant secondary redistribution of the material (as shown in [19]) and even to emission of secondary thermoelastic waves. In multipulse irradiation regimes, we can significantly affect the general pattern of the material modification by controlling the time separation between the pulses and thus achieving the desired states of the material [19]. Figure 1 shows the characteristic time scales of the response of the transparent material irradiated by femtosecond laser pulses.
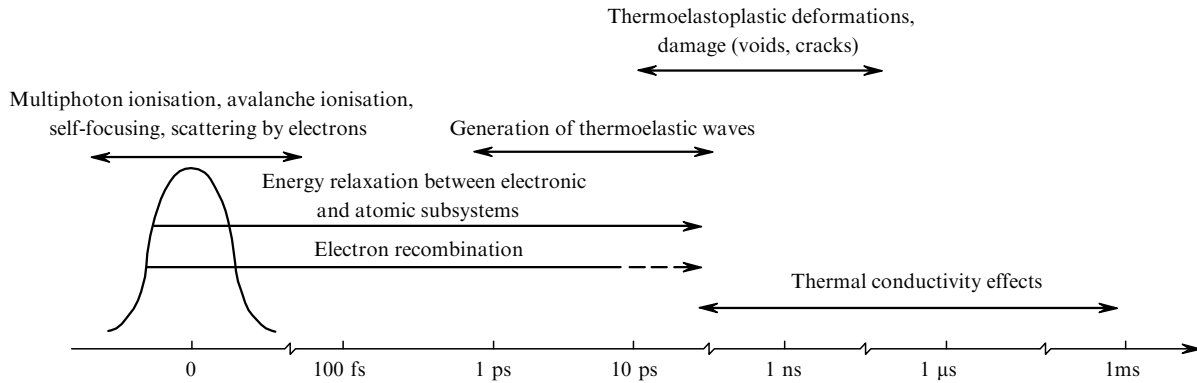
Figure 1. Characteristic time scales of various processes caused by irradiation of a transparent dielectric by a femtosecond laser pulse.

At present, most theoretical investigations are aimed at studying the mechanisms of plasma generation in crystals and glasses, the plasma dynamics and relaxation. The main mechanisms involved in generation of free carriers in dielectrics irradiated by visible and near-IR femtosecond laser pulses are the mutiphoton and avalanche ionisations [27–29]. At a power density of $\sim 5 \times 10^{13}$ W cm^{-2}, the tunnel ionisation starts to dominate in generation of free carriers [30, 31]. However, it can play a significant role only in the surface layer of the material because at focusing into the material bulk, radiation losses caused by photoexcitation and absorption in the generated plasma lead to the power intensity at a level when the mechanism of multiphoton ionisation prevails (clamping effect) [32, 33]. The role of avalanche ionisation in the breakdown of dielectrics irradiated by ultrashort laser pulses [34–37] – from complete negation of its existence for subpicosecond pulses [36] to assertion that this effect increases with decreasing pulse duration due to a decrease in the potential barrier in a strong field of a wave (cold avalanche) [37] – is still being debated. A better consent is achieved in regard of the electron recombination proceeding in dielectrics in the form of trapping in localised states, accompanied by the formation of colour centres, excitons and other defects [38–40]. Defect generation leads to incubation effects, for example, to a decrease in the breakdown threshold in the case of a train of laser pulses in multipulse operation regimes [40]. We can however expect that incubation, i.e., accumulation of defects and their preferential ionisation, can appear during the pulse action, increasing by the end of the pulse when the pulse duration exceeds the characteristic recombination time τ_{tr}. Thus, for fused silica we have $\tau_{tr} \approx 150$ fs [41] and can conjecture that a decrease in the 'fitting' values of the avalanche coefficient with increasing the pulse duration [37] is conditioned by secondary excitation of electrons trapped in defect states. The effects associated with heat buildup in the irradiation zone and with redistribution of the material under the action of thermoelastic and shock waves are poorly studied although heat accumulation often leads to irreversible changes in the dielectric structure [16, 42] while the action of stress waves leads to significant redistributions of the material density [19], to amorphisation in crystals, and to formation of voids and cracks [10, 20–23]. Some papers indicate that it is possible to achieve supercritical states and pressures ~ 10 TPa [22].

This review presents our recent works devoted to investigation of processes taking place upon irradiation of dielectric materials by 800-nm femtosecond laser pulses. We consider materials that are important in many optical technologies, for example, fused silica (in particular, doped ULE glass) and sapphire.

This review is organised as follows. In sections 2–4, we consider the conditions of radiation focusing on the material surface. Section 2 presents the basic equations used to describe photoexcitation of transparent materials at comparatively large spatial and time scales, which make it possible to trace the formation of a skin-layer in the breakdown, dynamic change in the optical properties, charging of the surface due to photoemission of electrons, and energy balance of the entire irradiation zone. Because of the extreme complexity of the problem, we give rather simplified equations, comment on the applicability of the assumptions and possible ways to improve model representations. In section 3, using the model representations we study the charging of the material surface layer irradiated by ultrashort laser pulses and show that electron photoemission can lead to a damage of the surface layer of the irradiated sample due to the electrostatic repulsive forces (Coulomb explosion). We demonstrate a self-consistent behaviour of electron photoemission in dielectrics, which leads to saturation of the photoemission current both with increasing laser fluence and decreasing pulse duration at a fixed fluence. In section 4, we consider the results of two-dimensional modelling, which make it possible to clarify the nature of characteristic differences in the shapes of craters produced on sapphire and fused silica surfaces irradiated by a train of ultrashort pulses. Section 5 is devoted to the issues of bulk modification of the materials when radiation is focused inside the sample. We analyse all the processes (from femtosecond photoexcitation to material cooling-down at times ~ 0.2 ms) ocurring in optical glasses during laser writing of waveguide structures. We show that it is possible to 'sew' the effects of photoexcitation and thermo-mechanical modifications in order to obtain a complete picture of the material evolution. Finally, in Conclusions we give a brief review of some surprising experimental facts, investigation and use of which can open up new possibilities in photonics and optoelectronics.

2. Photoexcitation and relaxation of transparent dielectrics irradiated by ultrashort laser pulses

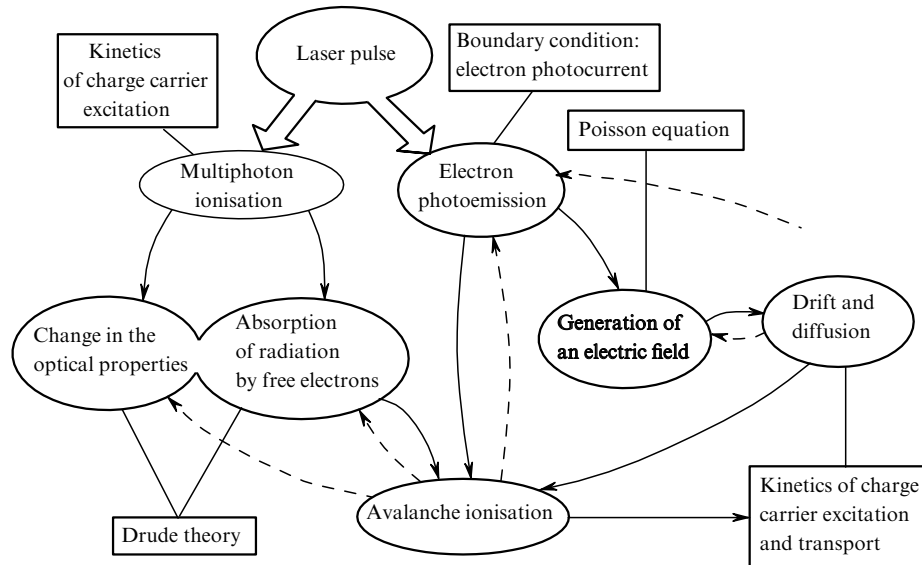As was mentioned in Introduction, laser radiation initiates

Figure 2. Schematic representation of laser-induced processes in dielectric materials (in ovals). The squares are the appropriate approaches to the description of the processes. Arrows show the main relations between various processes (solid lines show direct effects, dashed lines – the reverse effects).

in dielectrics many processes proceeding at different time scales. In this section, we analyse processes during ultra-short pulses and after the pulse action at the stage of relaxation of electron excitation. We consider the case of radiation focusing on the sample surface, which assumes the possibility of electron photoemission, accompanied by generation of electric fields and induced currents.

The theoretical description of the laser-induced dynamics of charge carriers is a complicated problem. Figure 2 presents a scheme demonstrating a correlation between various processes, which can be conditionally divided into two branches. One branch, beginning with the photo-ionisation process, is more universal and does not depend on the fact whether radiation is focused on the material surface or in its bulk. The second branch corresponds to the conditions of radiation focusing on the sample surface and begins with the electron photoemission. Most processes are mutually interrelated, which is shown by arrows.

Thus, multiphoton ionisation, whose order is determined by the ratio between the band gap width E_g and photon energy $\hbar\omega$, results in excitation of electrons from the valence band to the conduction band. These free electrons efficiently absorb laser radiation due to the bremsstrahlung, and in the case of the sufficiently absorbed energy, they can ionise neutral atoms of the material in collisions. The development of avalanche (collisional) ionisation accompanied by a drastic increase in the free electron concentration changes the optical properties of the material. In turn, the electron photoemission violates the quasi-neutrality of the irradiated sample when the positive charge is accumulated on the surface layer and a self-consistent electric field is produced. Under the action of the field, the electrons are redistributed, tending to neutralise the excess charge in the target 'body'. Due to the electron current, the positive charge is localised in the surface layer of the irradiated material in accordance with the balance between the diffusive and drift components of the current. The charge redistribution in the surface layer of the irradiated material affects photoemission and ava-lanche processes. At the same time, photoemission leads to

electron depletion in the surface layer and thereby decreases the avalanche efficiency in the depleted region. After the end of the laser pulse, electrons recombine, being trapped in excited localised states.

As shown in [43–46], the above correlation between the processes can be adequately described within the drift-diffusion approach, the main points of which are listed below. Note that this description, being quite laborious, is largely simplified. Thus, we use a simple expression for the multiphoton ionisation rate [28, 29] without the dependence of the effective electron mass on the quasi-momentum [47]. The development of avalanche ionisation is described by an empirical expression [29]. In recent years, some interesting approaches, for example, kinetics of radiation absorption by free electrons implying sequential levels [multiple rate equation (MRI)] [48], or a more rigorous approach based on the time-dependent Schrödinger equation [49] have been proposed to describe the development of avalanche ionisa-tion in dielectrics. However, for various reasons (the need to consider the surface layer of the sample of thickness on the order of the irradiation spot radius, in which the free electron density may experience sharp gradients; the dynamic behaviour of the reflection coefficient, which depends on the distribution of free electrons in the surface layer; etc.) the use of these approaches for self-consistent description of laser-induced excitation dynamics, transport and energy of charge carriers in dielectrics is not currently technically possible and reasonable in view of a sharp increase in awkwardness and complexity of this extremely complicated model.

2.1 Excitation and relaxation dynamics of a 'solid' plasma and its optical response

In transparent dielectrics with a wide band gap, absorption of the laser pulse energy can be divided into two stages. At the initial stage, free electrons are generated via the multiphoton ionisation, and the avalanche (collisional) ionisation develops when some 'seed' free-electron density is achieved. As noted above, at sufficiently high laser

radiation intensities the tunnelling ionisation may become dominant, as determined by the Keldysh parameter $\gamma = \omega\sqrt{2m_{\mathrm{eff}}E_{\mathrm{g}}}/(eE_{\mathrm{L}})$ (m_{eff} and e are the effective electron mass and charge, respectively; E_{L} is the electric field of the laser wave; E_{g} is the band gap width in a dielectric or ionisation potential of individual atoms and molecules) [30, 31, 47, 50]. In fact, the Keldysh parameter is a ratio of the characteristic time that an electron takes to overcome the energy barrier (the ionisation potential with allowance for its correction in the strong-wave field) to the electromagnetic-wave period. At $\gamma \gg 1$, the multiphoton ionisation mechanism prevails, while at $\gamma \ll 1$, the tunnelling one. It is assumed that for the tunnelling ionisation to produce a noticeable effect, the condition $\gamma < 0.5$ should be met; although, there are some experimental facts that point to the dominance of multiphoton ionisation already at $\gamma \ll 1$. These facts have led to numerous generalisations of the Keldysh theory for ionisation of dielectrics [47], as well as for atoms and molecules in the gas phase [50].

Note that for the radiation intensity $I_0 = 10^{14}$ W cm^{-2}, the parameter $\gamma \approx 0.85$ (assuming that m_{eff} is equal to the electron mass in vacuum m_{e}). Because in most irradiation regimes interesting to us $I_0 \leqslant 10^{14}$ W cm^{-2}, we will describe the excitation of electrons by using a simplified equation [28, 29]

$$\frac{\partial n_{\mathrm{e}}}{\partial t} = (W_{\mathrm{mph}} + Q_{\mathrm{av}})\frac{n_{\mathrm{a}}}{n_{\mathrm{lat}}} - \frac{n_{\mathrm{e}}}{\tau_{\mathrm{tr}}}. \tag{1}$$

Here, $W_{\mathrm{mph}} = \sigma_m I^m$ is the rate of multiphoton ionisation with an order m and cross section σ_m; $m = E_{\mathrm{g}}/\hbar\omega + 1$ (for sapphire and fused silica $E_{\mathrm{g}} \approx 9$ eV, and thus $m = 6$ at 800 nm); $Q_{\mathrm{av}} = \alpha I n_{\mathrm{e}}$ is the avalanche ionisation rate; α is the avalanche ionisation coefficient. The last term in (1) describes the electron recombination with a characteristic time τ_{tr}. Note that in this expression the ionisation terms are corrected to take into account a decrease in the density of neutral atoms n_{a} (n_{lat} is the concentration of atoms in the unperturbed sample), which may be important in achieving considerable degrees of ionisation (e.g., under conditions of the Coulomb explosion [43–46]). Temporal laser pulse shape can be described by a Gaussian:

$$I(t) = [1 - R(t)]\frac{2F_0}{\tau_{\mathrm{L}}}\sqrt{\frac{\ln 2}{\pi}}\exp\left[-4\ln 2\left(\frac{t}{\tau_{\mathrm{L}}}\right)^2\right], \tag{2}$$

where F_0 is the pulse fluence; τ_{L} is the pulse duration (full width at half maximum); R is the material reflectivity, which is a strong function of free-electron concentration. The optical properties of a dielectric irradiated by a high-power laser pulse, leading to a breakdown and metallisation of the irradiation zone, are calculated based on the Drude theory and the Fresnel formulas. The complex permittivity $\varepsilon^*(n_{\mathrm{e}})$ can be written as the contributions from the unexcited sample and the response of free-electron gas in the form [29, 51]

$$\varepsilon^*(n_{\mathrm{e}}) \simeq 1 + (\varepsilon_{\mathrm{g}} - 1)\left(1 - \frac{n_{\mathrm{e}}}{n_{\mathrm{e0}}}\right) - \frac{n_{\mathrm{e}}}{n_{\mathrm{cr}}}\left(1 + \mathrm{i}\frac{1}{\omega\tau_{\mathrm{c}}}\right)^{-1}. \tag{3}$$

Here, ε_{g} is the permittivity of the unperturbed sample ($\varepsilon_{\mathrm{g}} = n^2$; $n = 1.75$ and 1.45 for sapphire and fused silica, respectively [52]); n_{e}, $n_{\mathrm{cr}} = \varepsilon_0 m_{\mathrm{e}}\omega^2/e^2$ and n_{e0} are the electron concentration in the conduction band, the critical

electron concentration ($n_{\mathrm{cr}} = 1.74 \times 10^{21}$ cm^{-3} at 800 nm in vacuum), and the valence electron concentration, respectively; τ_{c} is the characteristic time of electron collisions (we assume that the damping factor is $\omega\tau_{\mathrm{c}} = 3$ [44]). To adequately describe the reflection dynamics at a dielectric breakdown, it is necessary to take into account the formation of the nonuniform profile of free electrons in the surface layer. To this end, we can use a multilayered reflection model [51], which consists in solving complex recurrence equations of the form

$$R_{i,k} = \frac{R_{i,i+1} + R_{i+1,k}\exp\left(-\mathrm{i}4\pi h_{i+1}\sqrt{\varepsilon_{i+1}}/\lambda\right)}{1 + R_{i,i+1}R_{i+1,k}\exp\left(-\mathrm{i}4\pi h_{i+1}\sqrt{\varepsilon_{i+1}}/\lambda\right)}, \tag{4}$$

where $R_{i,k}$ is the reflectivity from the layer consisting of layers from i to k; h_{i+1} is the thickness of the $(i+1)$th layer.

Dynamics of the free-electron distribution inside the irradiated sample is directly related to the local intensity of the electromagnetic wave whose attenuation in the material is determined by losses in the multiphoton ionisation and inverse bremsstrahlung absorption, and is described by the equation

$$\frac{\partial I(z,t)}{\partial z} = -W_{\mathrm{mph}}\frac{n_{\mathrm{a}}}{n_{\mathrm{lat}}}\hbar\omega m - a_{\mathrm{ab}}(z,t)I(z,t), \tag{5}$$

where $a_{\mathrm{ab}}(z,t)$ is the bremsstrahlung absorption coefficient calculated with the help of complex permittivity (3); z is the distance from the surface inside the sample. Note that the authors of [43–46] used the damping factor $\omega\tau_{\mathrm{c}} = 3$ yielding the $\sim 70\,\%$ reflectivity for supercritical electron concentrations, in agreement with experimental data [53].

2.2 Electron photoemission, self-consistent electric field, drift, and diffusion

When processing the surface by ultrashort pulses, an abrupt ejection of electrons from the surface in the course of photoemission can lead to far-reaching consequences, such as material ablation before reaching the melting point of the material (the Coulomb explosion mechanism) [43–46], a significant influence on the material ablation dynamics of the electronic cloud over the surface [54], acceleration of ions emitted from the surface. It can occur at photoemission currents that are already lower than the threshold current of the Coulomb explosion [54, 55]. Thus, for typical conditions of the Coulomb explosion, the material ablation leads to the formation of a smooth surface without any traces of melting [56], which can be used for ultrafine laser surface processing. Recall that the Coulomb explosion is a mechanism of laser ablation, in which due to the effective electron photoemission in the material surface layer an excess positive charge is produced, which is sufficient to desintegrate this layer by the electrostatic repulsion of the ions.

Papers [43–46] showed that the Coulomb explosion mechanism is realised under certain conditions of irradiation of dielectric materials in the surface layer of which a significant positive charge is accumulated due to the low mobility of electrons and the spatial limitation of the breakdown zone. The issue of the Coulomb explosion of semiconductor and metal materials is still being actively discussed [55, 57]. The criterion of the Coulomb explosion is the excess of the energy of the quasi-static electric field

produced by an excess positive charge over the binding energy of surface atoms of the irradiated sample. This condition can be written in the form [45]:

$$E_{th}|_{z=0} = \sqrt{\frac{2(\Lambda_{at} - 3kT_{lat})n_{lat}}{\varepsilon\varepsilon_0}}. \qquad (6)$$

Here, E_{th} is the threshold electric field that is necessary to initiate the Coulomb explosion mechanism; Λ_{at} is the binding energy of atoms in the lattice per atom; T_{lat} is the temperature of the 'heavy' component of the sample (the lattice for crystals and the molecular 'matrix' in glasses). Note that condition (6) may be too rigid, because the ionised material (the electron–hole plasma) is characterised by the so-called softening of the bonds due to their partial rupture. Nevertheless, condition (6) should correctly predict the magnitude of the electric field, which can result in a macroscopic Coulomb explosion (ablation of at least several monolayers rather than a probabilistic emission of individual ions from the surface).

To describe the laser-induced charging of the material surface, equation (1) should be substantially modified to take into account electron photoemission from the surface layer of the irradiated sample and the electron transport under the action of a forming self-consistent electric field. In this case, equation (1) takes the form

$$\frac{\partial n_e}{\partial t} + \frac{1}{e}\frac{\partial J_e}{\partial z} = (W_{mph} + Q_{av})\frac{n_a}{n_{lat}} - \frac{n_e}{\tau_{tr}} - PE, \qquad (7)$$

where PE is a term describing photoemission of electrons from the surface layer of the target; J_e is the induced electron current density in the sample. The expression for the current density of the form $J_e = en_e v_e$ (v_e is the directed velocity of electrons) can be written in the drift-diffusion approximation:

$$J_e = -en_e\mu_e E - eD_e\nabla n_e. \qquad (8)$$

The time-dependent diffusion coefficient D_e can be calculated according to the Einstein relation: $D_e = k_B T_e \times \mu_e/|e|$, where μ_e and T_e are the electron mobility and temperature; k_B is the Boltzmann constant. The electric field E, which arises in the sample because the quasi-neutrality is violated due to the electron photoemission, is determined with the Poisson equation by the difference of local concentrations of ions n_i and electrons n_e:

$$\frac{\partial E}{\partial z} = \frac{|e|}{\varepsilon\varepsilon_0}(n_i - n_e). \qquad (9)$$

Note that against the background of the electromagnetic-wave field, this field is quasi-static.

The description of the photoemission term $PE(z, t)$ in (7) is a challenging problem. Our model is based on the assumption of a statistical distribution of free-electron momenta in wide band-gap dielectrics, in which the conduction band minimum is at the level of the vacuum, so that the electrons residing close to the surface and having a momentum component directed toward the vacuum, can leave the sample. Thus, we suggest that due to the instantaneous angular momentum distribution, half the

free electrons in average produced in the multiphoton and collisional ionisation are immediately emitted from the surface and a thin surface layer of thickness l_{PE} (for dielectrics we can set $l_{PE} \sim 1$ nm [58]). We assume that photoemission occurs with the highest probability directly from the surface, this probability decreasing exponentially towards the bulk of the material. Thus, we can write:

$$PE(z, t) = \frac{1}{2}(W_{mph} + Q_{av})\frac{n_a}{n_{lat}}\exp\left(-\frac{z}{l_{PE}}\right). \qquad (10)$$

As we have shown, such a construction of the photoemission term yields in simulations the integrated photoemission current, which agrees well with experimental data for dielectrics [59].

2.3 Simplified energy representation

An important issue in modelling the effect of the ultrashort laser pulses on dielectrics is to describe the dynamics of their heating and melting (in the case of amorphous materials, softening). In addition, because the electron diffusion coefficient depends on the temperature (energy), the energy representation is also important for considering the cases below the melting point when ablation resulting from the Coulomb explosion dominates. To describe the dielectric heating dynamics, we used a simplified representation based on a two-temperature model [60, 61] under the assumption that a highly ionised dielectric can be treated as a two-temperature plasma:

$$C_e\left(\frac{\partial T_e}{\partial t} + \frac{J_e}{en_e}\frac{\partial T_e}{\partial z}\right) = \frac{\partial}{\partial z}K_e\frac{\partial T_e}{\partial z}$$
$$- g(T_e - T_{lat}) + \Sigma(z, t), \qquad (11)$$

$$[C_{lat} + L_{melt}\delta(T_{lat} - T_{melt})]\frac{\partial T_{lat}}{\partial t}$$
$$= \frac{\partial}{\partial z}K_{lat}\frac{\partial T_{lat}}{\partial z} + g(T_e - T_{lat}). \qquad (12)$$

Using the Boltzmann equation, Kaiser et al. [31] showed that already after ~ 20 fs from the onset of laser irradiation of the target made of fused silica, the electron energy distribution is fairly smooth, with a barely perceptible peak at low energies. Thus, even if the complete equilibrium is not reached within the electronic subsystem, the value of T_e can be considered as a measure of the average electron energy. In equations (11) and (12), C_e, C_{lat} and K_e, K_{lat} are the heat capacities and thermal conductivities of the electron and lattice subsystems, respectively (for convenience, we use here the term 'lattice' for amorphous substances, implying the atomic core of the material); g is the electron–lattice relaxation constant; $\Sigma(z, t)$ is a term describing the laser pulse energy absorption. Note that we introduced two additional terms in the two-temperature model equations; the first term describes the energy transfer due to the electron current (11), while the second term of the form $L_{melt}\delta(T_{lat} - T_{melt})$ in equation (12) allows the pass-through calculation of the melting boundary propagation (T_{melt} and L_{melt} are the melting temperature and heat, respectively; δ is the δ-function). It is worth mentioning that in the presence of ultrafast processes, the solid material can be significantly superheated to a

temperature above the melting point [62, 63], which, however, has not been investigated for dielectric materials and is beyond the scope of the works presented here.

The laser energy source in equation (11) is based on a detailed consideration of the energy balance of the electrons. The balance includes the initial energy of free electrons produced in multiphoton ionisation, the energy spent on the development of avalanche ionisation, inverse bremsstrahlung absorption of radiation, and the energy localised upon electron trapping and carried away by photoelectrons from the sample. Thus, the change in the total kinetic energy E_f of the electron subsystem can be written as

$$\frac{\partial E_f}{\partial t} = (m\hbar\omega - E_g)W_{mph}\frac{n_a}{n_{lat}} - E_g Q_{av}\frac{n_a}{n_{lat}} + a_{ab}I(z,t)$$

$$- E_e\frac{n_e}{\tau_{tr}} - E_e PE(z,t). \quad (13)$$

Here, E_e is the average kinetic energy per electron (we assume that $E_e = 3k_B T_e/2$). The laser energy source in equation (1) has the form:

$$\Sigma(z,t) = n_e\frac{\partial E_e}{\partial t} = \frac{\partial E_f}{\partial t} - \frac{3}{2}k_B T_e\frac{\partial n_e}{\partial t}. \quad (14)$$

The thermodynamic parameters of the electron subsystem can be represented as follows: $C_e = 3k_B n_e/2$, $K_e = 2k_B^2 \mu_e \times n_e T_e/e$ [64]. For ultrashort times of the order of ~ 1 ps and ~ 10 ps in the process of laser-induced charging of the sample and in the shaping problem, respectively (see Section 4), the lattice thermal conductivity can be neglected. The value of g can be determined from the known data on the characteristic times of electron–lattice relaxation τ_r as $g = C_e/\tau_r$ (for transparent dielectrics $\tau_r \sim 1$ ps).

As boundary conditions, we use Gauss' law for the Poisson equation and the free inflow of electrons through a boundary of the computation domain inside the sample. The depth of the computation domain was chosen less than or approximately equal to the radius of the irradiation spot. If the computation domain is larger than 1 μm, we observed only a small change in the time of the charge confinement on the surface [45], the main features of the charging process being preserved. Equations (2)–(14) with these boundary conditions are basic for the model developed in [43–45] and used to describe the effects of laser-induced charging [43–46, 65] (see Section 3) and the shaping of craters [65, 66] (Section 4) on the dielectric surfaces.

3. Laser-induced charging of the surface and a Coulomb explosion

3.1 Modelling and experiment

It has been sufficiently long known that, depending on irradiation conditions, two scenarios of laser ablation of sapphire (Al_2O_3) are possible: 'gentle' ablation, when a layer of several nanometres in thickness is removed from the material surface, and 'strong' ablation characterised by a sharp increase in the thickness of the ablated layer [56, 67–70]. Gentle ablation is typical of irradiation regimes, when the laser fluence only slightly exceeds the ablation threshold at a small number of pulses irradiating a fixed spot on the sample surface. In this case, the material surface after ablation becomes smooth, often much

smoother than the surface of the original sample (Fig. 3a). Either with increasing the laser pulse fluence or with increasing the number of pulses at a relatively low fluence, the strong ablation regime starts to dominate (Fig. 3b), when after irradiation we can observe on the surface characteristic traces of melting, the melt spread, and explosive 'boiling' (the so-called phase explosion [71, 72]). Analysis of the experimental data shows that upon irradiation of dielectric materials by ultrashort pulses with the fluence near the ablation threshold, the material ejection from the surface has features that indicate an electrostatic ablation mechanism. First, the degree of ionisation of ablation products and their velocity distributions for gentle and strong ablation differ considerably. In the case of gentle ablation, ions, which are the main component of the ablation products, have a narrow angular distribution along the normal to the surface and a high ($\sim 2 \times 10^4$ m s^{-1}) average directed velocity. In passing to strong ablation the angular distribution of ions becomes wider, and their characteristic velocity is $\sim 1.2 \times 10^4$ m s^{-1}, which corresponds to the thermal velocity of evaporated particles [56]. Moreover, in the case of gentle ablation, different ionic components of the plume (Al^+ and O^+) have the same momentum that is independent of mass (Fig. 3c), whereas in the case of strong ablation, they tend to have the same energy [56, 70]. A more pronounced difference is observed in the behaviour of F^+ and F^- ions in the case of gentle ablation of barium fluoride, when negative ions considerably slow down relative to the positively charged particles [73].
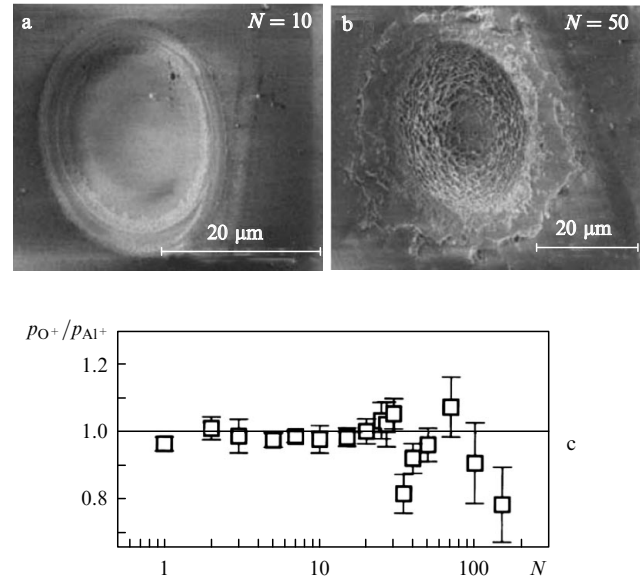

Figure 3. Sapphire surface in passing from gentle (a) to strong (b) ablation with increasing the number of laser pulses N (200 fs, 4 J cm^{-2}); (c) ratio of the momenta of oxygen ions to aluminium ions, calculated by the distribution maxima of their velocities [70].

These facts suggest that in the gentle ablation regime there exists a mechanism of ion acceleration by an electric field generated in the laser-irradiated target. The reasons for the neutrality violation of the irradiated material, which lead to the formation of the field, are a significant electron photoemission from the surface and a decrease in the

transfer rate of hot electrons in the target for neutralising the excess charge.

The model described in Section 2, allowed us to study the dynamics of charge carriers in irradiated materials and to draw important conclusions about the physical processes responsible for the accumulation of the excess charge in the surface layer of the irradiated sample, and the possible consequences of this phenomenon. Note that this model is quite versatile, and with a corresponding change in some of its parameters and in its mechanisms (absorption of laser radiation, description of generation and relaxation of charge carriers, form of the photoemission term) it can be used for any type of material [43–45]. Comparative modelling performed for dielectrics, semiconductors, and metals (we used Al_2O_3, Si, and Au as typical representatives of their classes) showed that in dielectrics at a laser pulse fluence near the ablation threshold the electric field induced by photoemission may exceed the threshold value (6), which speaks in favour of the Coulomb explosion mechanism [43–45]. At the same time, due to high carrier mobility, the Coulomb explosion is unlikely in semiconductors and metals, because the generated electric fields are several orders lower than the corresponding thresholds.

Calculations show that the electric field on the surface of the irradiated material reaches a maximum during the pulse action; after it, the field gradually decreases due to the charge inflow to the surface from the sample bulk. Figure 4 shows the spatial distributions of the electric field in the Al_2O_3, Si and Au targets when the field reaches the peak value under experimental conditions of papers [43, 56] (wavelength, 800 nm; pulse duration, 100 fs). The laser pulse fluence corresponds to the thresholds at which a significant amount of ions (4, 0.8, and 1.2 J cm^{-2} for Al_2O_3, Si, and Au, respectively) appear in the time-of-flight distributions of ablation products. The thresholds of the electric field E_{th}, estimated by the latent heat of vaporisation per particle for cold materials, are equal to $\sim 5 \times 10^{10}$ (Al_2O_3), 2.65×10^{10} (Si), and 2.76×10^{10} V m^{-1} (Au). Only in sapphire, the generated electric field considerably exceeds the threshold. Moreover, the thickness of the layer with the above-threshold field, where the material should break down due to the forces of electrostatic repulsion (i.e., the Coulomb explosion should take place)
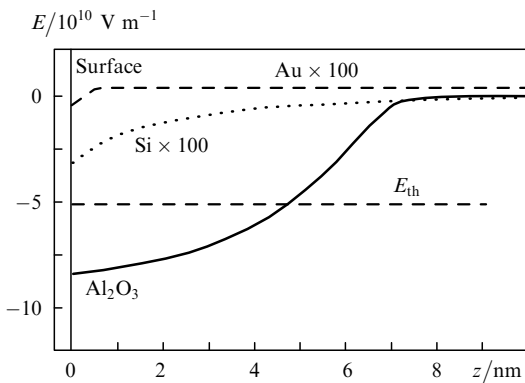

Figure 4. Spatial profiles of electric fields in the targets of sapphire, silicon, and gold at the time of reaching their maximum values, calculated for experimental conditions [43, 56]. The fluences of 100-fs laser pulses at a wavelength of 800 nm correspond to the thresholds of ion emission for each material (4, 0.8, and 1.2 J cm^{-2} for Al_2O_3, Si, and Au, respectively).

is equal to ~ 40 Å, in excellent agreement with experimental observations [56]. In silicon and gold, the high mobility of free charge carriers results in accumulation of a considerably lower positive charge on the sample surface, this charge being insufficient to initiate the Coulomb explosion. The maximum values of electric fields for the conditions of Fig. 4 are 4.1×10^7 (gold) and 3.4×10^8 V m^{-1} (Si).

It is worth noting a few important facts. At a high pulse fluence, when the thermal ablation regime dominates and the developed plasma plume is produced, ions observed in the plume also often have the same momentum. However, we cannot assert definitely that these ions emerged as a result of the Coulomb explosion of the material surface layer, because they can accelerate by separating the charge in the expanding plasma (formation of a double layer) [74, 75]. Experimental confirmation of the Coulomb explosion in metals was obtained only under extreme intensities ($\sim 10^{19}$ W cm^{-2}) of the laser pulse acting on the tantalum wire 50 μm in diameter [76]. When the pulse fluence is below the melting threshold, the observed emission of the individual ions from the metals can be explained by the optical rectification mechanism [77]. The electronic mechanism of ion emission from silicon surfaces was studied in [78, 79] for nanosecond laser pulses in the UV wavelength range. However, it should be noted that only transparent dielectrics have the properties that lead to accumulation of a large charge on the surfaces irradiated by ultrashort pulses. Moreover, as will be shown below, the charge accumulation in the dielectric surface layer leads to photoemission saturation and limits the Coulomb ablation depth.

3.2 Photoemission saturation effect

We consider the influence of the irradiation conditions (fluence and pulse duration) on formation of a laser-induced electric field in dielectrics when the melting threshold is not achieved (gentle ablation). We present the results of modelling for sapphire and doped fused silica (ULE), consisting of SiO_2 (92.5 %) and TiO_2 (7.5 %). Parameters of the materials used in modelling are listed below.

	Sapphire	ULE
Atom concentration		
$n_{lat} = n_a + n_i$/cm^{-3}	1.17×10^{23}	6.4×10^{22}
Valence electron concentration		
n_{e0}/cm^{-3}	5.6×10^{23}	3.4×10^{23}
Band gap width E_g/eV	9	9
Multiphoton ionisation coefficient		
σ_6/cm^{-3} ps^{-1} (cm^2 TW^{-1})^6	8×10^9	6×10^8
Avalanche ionisation coefficient		
α/cm^2 J^{-1}	6	4
Refractive index n	3.0983	3.99
Electron mobility μ_e/m^2 V^{-1} s^{-1}	3×10^{-5}	3×10^{-5}
Time of electron recombination		
(trapping) t_{tr}/s	10^{-10}	0.15×10^{-12}
Characteristic relaxation time τ_r/s	10^{-12}	10^{-12}

Because some ULE parameters are unknown, we used in the modelling the known data for fused silica (the coefficients of multiphoton and avalanche ionisation are taken from [80]). The electron mobility for sapphire and ULE was assumed the same on the basis of the observations [81], with corrections for a dense excited plasma [44, 82].

The electric field in sapphire, represented in Fig. 4, was obtained for the total number of electrons $\sim 7 \times 10^8$, emitted from the irradiated spot with the area $S_{ir} = 470$ μm^2 [44]. This photoelectron current is in good agreement with the experimental values for dielectric materials [59]. Figure 5a presents the dependence of the photoelectron yield from the sapphire surface on the pulse fluence (wavelength, 800 nm; duration, 100 fs; the time-integrated electron current density from the surface multiplied by the irradiation spot area, 470 μm^2). Obviously, the charging of the surface increases the work function of electrons [83]. Although this effect is neglected in our model, we still observe the self-regulation of photoemission above some fluence (~ 3.5 J cm^{-2} for 100-fs pulses). At such fluences, strong photoemission of electrons in active multiphoton ionisation in the laser pulse maximum leads to the depletion of electrons in the material surface layer (within the photoemission layer of thickness l_{PE}). As a result, the efficiency of avalanche ionisation in this layer decreases and, starting with some fluence, the total yield of photoelectrons tends to saturate (Fig. 5a). Interestingly, in modelling the fluence in the case of photoemission saturation virtually coincides with the experimentally determined threshold of the Coulomb explosion, which for sapphire is slightly below 4 J cm^{-2} [43]. Due to saturation of the photoelectron yield, the maximum electric field, generated on the material surface, only weakly increases with the laser pulse fluence (Fig. 5b).
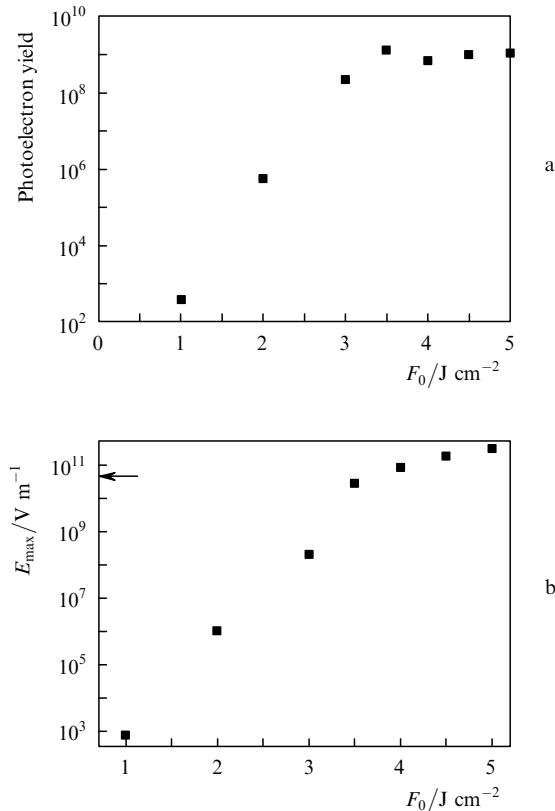
The same features of surface charging were obtained in modelling the ULE irradiation, where the self-regulation effect of electron photoemission for 100-fs pulses is observed starting with 5.2 J cm^{-2}, and as we might expect the self-regulation 'threshold' decreases with decreasing the pulse duration (~ 3.2 J cm^{-2} for 30-fs pulses). The process of surface charging has also a clear tendency to saturate (Fig. 6). This figure shows the time evolution of the excess charge on the ULE surface for 100- and 30-fs pulses. When the fluence increases from 5 to 5.5 J cm^{-2} (Fig. 6a), the charging amplitude increases by approximately 10 times, whereas the fluence further increases by 0.5 J cm^{-2}, the effect of the increasing excess charge is markedly less pronounced. Moreover, in the case of shorter laser pulses (Fig. 6b) with the fluence above the Coulomb explosion threshold, the charging peak increases with the pulse fluence, the field pulse becoming shorter. We note another interesting feature of the surface charging of dielectrics: its peak is observed at the end of the laser pulse, which is due to the mentioned delay of avalanche ionisation.
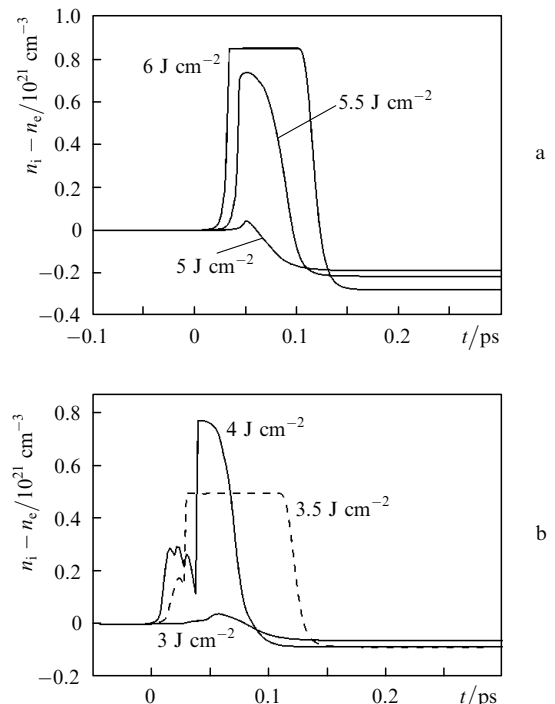
Figure 6. Time evolution of the excess charge on the ULE surface irradiated by 100- (a) and 30-fs (b) pulses with different fluences at a wavelength of 800 nm [46]. Maximum of the laser pulse corresponds to $t = 0$.

Interestingly, the estimated depth of the above-threshold (supercritical) electric field penetration in the material does not exceed $4-5$ nm, regardless of the pulse fluence, which is the result of the electron photoemission saturation. Thus, the layer thickness of the material emitted from the surface due to the Coulomb explosion does not exceed a few nanometres. For the case shown in Fig. 5, the material melts at $F_0 \geqslant 5$ J cm^{-2}. If the surface is damaged at subpicosecond durations due to the Coulomb explosion, the signs of the Coulomb explosion are concealed (see Fig. 3b) during material melting and subsequent strong ablation (thermal or thermomechanical [84]). Figure 7 represents the effect of limitation in the Coulomb explosion

Figure 5. Number of photoelectrons leaving the sapphire surface during the laser pulse (a), and the maximum value of the electric field formed on the sample surface during irradiation (b) as functions of the fluence per pulse [46]. The pulse duration is 100 fs and the area of the irradiation spot is 470 μm^2. The critical field necessary for the Coulomb explosion is shown by the arrow.

depth, accompanied by a sharp threshold effect of formation of a supercritical field in the sample. With increasing the pulse fluence from 3 to 3.5 J cm^{-2}, the field increases sharply from the considerably subthreshold one to that exceeding the threshold value by four times (the estimated threshold field for the ULE is $\sim 4.5 \times 10^{10}$ V m^{-1}). A further increase in the fluence up to 4 J cm^{-2} almost does not change the behaviour of the electric field either in time (Fig. 7a) or in space (Fig. 7b). This indicates a very narrow range of irradiation conditions in which the Coulomb explosion mechanism can be effectively used for ultraprecise treatment of transparent materials. Note that for shorter pulses the lifetime of the above-threshold electric field tends to increase, which also increases the probability of the Coulomb explosion in dielectrics.
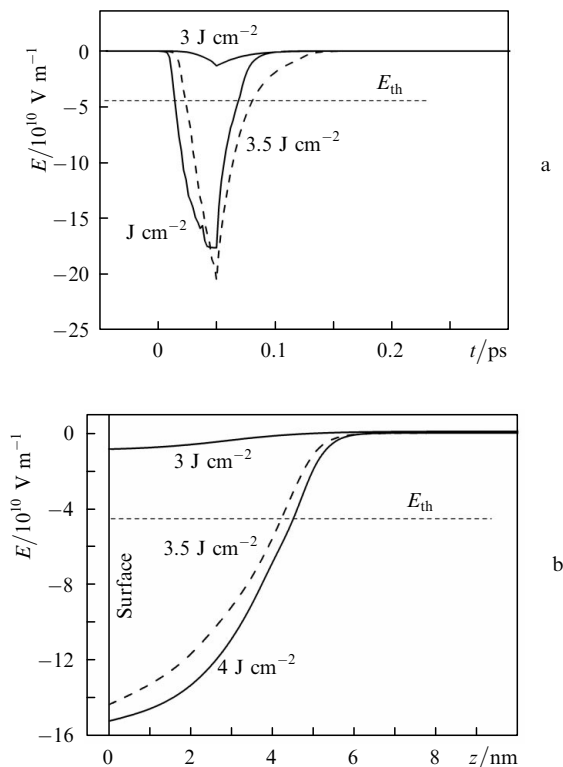

Figure 7. Time evolution of the electric field strength formed on the ULE surface (a) and spatial (in-depth) distribution of the electric field strength at a time instant of 30 fs after the maximum of the laser pulse (the maximum coincides with $t = 0$) (b). The irradiation conditions are the same as in Fig. 6b (according to [46]).

4. Two-dimensional modelling: crater shaping

We discussed above mostly the processes taking place in transparent materials under conditions when their melting/softening threshold is not reached. Here we will touch on the issues of modelling more severe irradiation conditions that lead to ablation of transparent materials. Although the above-described model is not intended to model the ablation process, i.e., material ejection from the surface, we will, however, show below that it allows one to analyse in detail the thermodynamic state of the material.

Adaptive temporal shaping of laser pulses by the Fourier synthesis of spectral components is a powerful tool of control over various physical and chemical systems which allow one to obtain the desired results [85, 86]. In particular, the adaptive control of laser pulse shape provides a unique opportunity to process transparent materials. By controlling the laser pulse duration we can synchronise the energy deposition into the material with its characteristic response to the input of energy. When the dielectric material is irradiated by a time-modulated laser pulse, the deposition of certain portions of energy can 'prepare' the irradiated surface or volume (for example, by producing a certain free-electron density or the phonon temperature) to the subsequent portions of the laser radiation, thus changing significantly the absorption process. Therefore, it is possible to reduce the stress arising in the material, to achieve cleaner processing or desired modification, which depends on the properties of a concrete material and is especially useful in the case of fragile samples.

Deep understanding of physical processes in dielectrics irradiated by time-modulated laser pulses, and their relationship can additionally help to optimise and control the micromachining technologies. The energy input in the irradiated sample depends on its ability to transform electronic excitation into vibrational modes or localised deformation states of the atoms involved in trapping of charge carriers. From this point of view, the two materials considered in this section differ significantly in the relaxation time of free electrons. In such materials as α-quartz (c-SiO$_2$), or fused silica (a-SiO$_2$), electrons are rapidly trapped (with characteristic time ~ 150 fs), accompanied by generation of relatively long-lived excitons (the characteristic lifetime of the order of several milliseconds [87]). In other oxides, such as sapphire (Al$_2$O$_3$) or magnesium oxide (MgO), free electrons are stored at the conduction band bottom up to several tens of picoseconds.

As shown in [88, 89], these features of the electron–lattice system can be used to improve the processing and structuring of the dielectric surface. The authors of [88, 89] showed in experiments that the use of specially time-modulated laser pulses makes it possible to produce craters of a spatially modulated shape on the fused silica surface. Using the adaptive equipment they obtained the designed laser pulses from a 800-nm Ti : sapphire laser, consisting of a train of three 100-fs pulses with a time separation of ~ 1 ps, which allowed them to produce step-like craters. With decreasing the time separation between the pulses, the crater modulation effect disappears. At the same time, the authors failed to obtain crater modulation on the sapphire surface under any irradiation conditions. The model we developed using the above-described drift-diffusion approach made it possible to shed light on the nature of laser-induced modulation of crater structures [66].

4.1 Some remarks on the model two-dimensionality; allowance for defect accumulation

The authors of [90–92] showed that by using numerical modelling we can not only analyse in detail the processes taking place in dielectrics irradiated by ultrashort laser pulses, but also predict the depth and shape of craters produced on the surfaces of the irradiated samples.

The developed two-dimensional model describes the laser energy absorption and transfer in dielectrics under pulsed laser radiation, in particular for pulses of a complex modulated spatiotemporal shape. The purpose of constructing this model involved modelling the spatial structure of the

electron system excitation of a dielectric under conditions typical of surface processing [88, 89]. The model made it possible to identify the basic physical processes responsible for the structure modulation and get additional information about the dynamics of optical breakdown in dielectrics, taking into account the temporal and spatial evolution of the free-electron concentration, the defect accumulation, the energy of the electron and lattice systems, and the optical response of the target irradiated by modulated laser pulses. Extending the one-dimensional model described in Section 2 to the two-dimensional case was motivated by the need for a direct comparison of modelling results with experimental data on the shapes of induced craters. Despite the fact that the radial energy transfer under the conditions when the irradiation spot radius is much greater than the depth of the optical breakdown does not play a noticeable role, the two-dimensional modelling in a single variant of calculations can help to describe all the spatial distribution of a laser pulse by the irradiation spot and avoid multivariate (step by step) series of one-dimensional calculations. In addition, the analysis of the data revealed that the modulations obtained in a series of one-dimensional calculations do not account for the effect of two-dimensional electronic conductivity, which tends to smooth the isolines of the temperature distribution, particularly in the intervals between successive pulses. The radial heat transfer (negligibly small on the scales of the irradiation spot) may be important on smaller scales of structure modulation.

Thus, the one-dimensional modelling can lead to an overestimation of the modulation parameters, which in the case of a more realistic two-dimensional approach can be significantly smoother or disappear completely. The two-dimensional modelling clearly demonstrates that it is the process of electron trapping with the formation of defect states and the associated dynamics of the optical properties of the plasma excited in the dielectric that plays a fundamental role in shaping the resultant spatial profile of the craters.

For the two-dimensional simulation, the model described in Section 2 was somewhat modified. Thus, energy transport equations (11) and (12) are written for the case of a cylindrically symmetric laser beam incident normally on the sample surface. Bulgakova et al. [92] demonstrated that the laser-induced current of charge carriers has very little effect on the final heating of the sample; therefore, the effects of surface charging, the electric field and electron current are not taken into account (the terms containing the field and current were ruled out from all equations). The equations of the charge carrier continuity are modified to account for the defect accumulation and have the form:

$$\frac{\partial n_{\mathrm{e}}}{\partial t} = (W_{\mathrm{mph}} + Q_{\mathrm{av}}) \frac{n_{\mathrm{a}}}{n_{\mathrm{lat}}} - \frac{n_{\mathrm{e}}}{\tau_{\mathrm{tr}}}, \tag{15}$$

$$\frac{\partial n_{\mathrm{d}}}{\partial t} = \frac{n_{\mathrm{e}}}{\tau_{\mathrm{tr}}}, \tag{16}$$

$$n_a = n_{\mathrm{lat}} - n_{\mathrm{e}} - n_{\mathrm{d}}, \tag{17}$$

where n_{d} is the defect concentration; we assume that $n_{\mathrm{i}} = n_{\mathrm{e}}$. Note that we do not take into account the ionisation of defects (produced after the first pulses) by subsequent pulses. However, this can be done while further

improving the model. Thus, in the case of fused silica, the formation of excitons is characterised by the absorption peak 5.2 eV [41] which, for $\lambda = 800$ nm means four-photon excitation process of trapped electrons back into the conduction band. Therefore, the term W_{mph} in equation (15) should take into account the rate of six-photon ionisation of neutral atoms and four-photon excitation of defects into the conduction band. It is known that the excitons in fused silica are small – on the order of atomic radius (~ 0.17 nm [87]). Because the data on their collisional ionisation are absent, we can obtain a qualitative picture by assuming that the cross section of their ionisation in collisions coincides with that of neutral atoms. Then, the term Q_{av} (together with the normalisation factor) should be also replaced by the term taking into account the avalanche ionisation of both atoms and excitons. Accordingly, we should modify heat balance equation (13). However, due to the absence of reliable data on the above constants, we will restrict our consideration here to the modelling neglecting the re-excitation of the trapped electrons back into the conduction band. The optical part of the model (Section 2) is unaltered, describing in this case the dynamics of the optical properties not only inside the material, but also over the irradiation spot radius. The two-dimensional model and modelling parameters are described in more detail in [66]. We below present the results of modelling for the experimental irradiation conditions of sapphire and fused silica [88, 89].

4.2 Thermodynamic analysis of two-dimensional heating dynamics: sapphire and fused silica

Assuming that the ejection of the material from the surface is limited by a certain level of its temperature reached during laser heating, above which the substance experiences a phase transition, the final shape of craters can be analysed based on isosurfaces of the temperature in the irradiated samples. It should be noted that in the case of a step-like shape of isosurfaces, the ejection of the material can lead to some smoothing of the crater bottom due to recoil forces. However, if the isosurfaces are smooth, it is difficult to expect a step-like shape of craters, as in experiments [88, 89]. Figure 8 shows the temperature isolines in the surface layer of sapphire and fused silica irradiated by a train of three identical 100-fs pulses separated by 1 ps. The total fluence amounts to 14 J cm^{-2}. Recall that the irradiation geometry is assumed cylindrical. In sapphire, oval smooth temperature isolines are formed, whereas in fused silica the isolines have some modulation with a tendency to deepen at the centre of the irradiation spot. The insets show for comparison the cross sections of the craters obtained in the experiments [89]. Obviously, the calculated temperature isolines and experimental crater shapes have in general common features. However, in Fig. 9, where the defect energy is added to the temperature of the sample [$T_{\mathrm{tot}} = T_{\mathrm{lat}} + E_{\mathrm{d}}/(3k_{\mathrm{B}}n_0)$], the modulations are more pronounced (see Figs 8b and 9a). The defect energy E_{d} is calculated by the equation

$$\frac{\partial E_{\mathrm{d}}}{\partial t} = E_{\mathrm{e}} \frac{n_{\mathrm{e}}}{\tau_{\mathrm{tr}}}. \tag{18}$$

Contribution of defects in the local accumulation of the energy [isolines $T_{\mathrm{d}} = E_{\mathrm{d}}/(3k_{\mathrm{B}}n_{\mathrm{lat}})$] is shown in Fig. 9b. One

can see that it is the defect accumulation that determines the observed modulation in fused silica. It should be emphasised that the defect concentration in sapphire is very low at time scales of a few picoseconds, and allowance for their energy in plotting the isoline does not change the pattern shown in Fig. 8. The shapes of the temperature isolines in sapphire do not depend on the time separation between pulses, and in simulations with a smaller (of the order of a few hundreds of femtoseconds) delay we obtained the same distribution as in Fig. 8. Moreover, in modelling for fused silica with a small time separation between the pulses (0.3–0.5 ps), we also obtained smooth oval craters without any traces of spatial modulation (see [66]), which indicates the decisive role of defects in the observed phenomenon.

Returning to Fig. 8, we note that in the central parts of the irradiation spot, a certain amount of the material (both

in sapphire and fused silica) is heated above the thermodynamic critical temperature T_{cr}. To estimate the T_{cr}, we can use one of the methods discussed in [72]. For most materials, the expected value of T_{cr} is one and half to two times higher than their boiling point under normal conditions (2270 K for SiO_2 and 3250 K for Al_2O_3 [93]). Consequently, we can expect that the critical temperature is ~ 4000 K for fused silica and 5000–6000 K for sapphire. According to thermodynamic concepts [72, 94, 95], the molten material during rapid heating to the T_{cr} experiences superheating to a metastable state and decays into vapour-droplet mixture. Moreover, the authors of [96, 97] suggested that in the case of the extremely rapid heating, as in the case of irradiation by ultrashort pulses, the superheated liquid material can cross the spinodal and undergo transition to the gas state, bypassing the droplet phase. We can roughly assume that the substance at a temperature above T_{cr} leaves
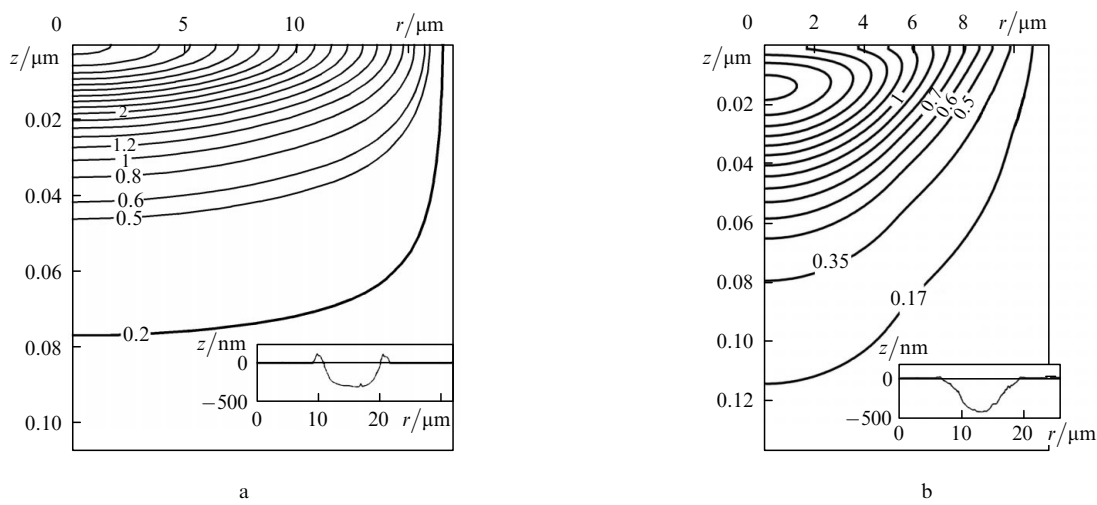
Figure 8. Temperature distributions in Al_2O_3 (a) and a-SiO_2 (b) targets after irradiation by a train of three identical 100-fs laser pulses (the time separation between pulses, 1 ps; the total energy density, 14 J cm^{-2}) at time instant of 3 ps relative to the maximum of the first pulse; r is the radius, z is the distance inside the material, $(r, z) = (0, 0)$ corresponds to the centre of the irradiation spot on the surface, the temperature levels are given in eV (from [66]). The insets show the cross sections of craters, obtained experimentally in [89].
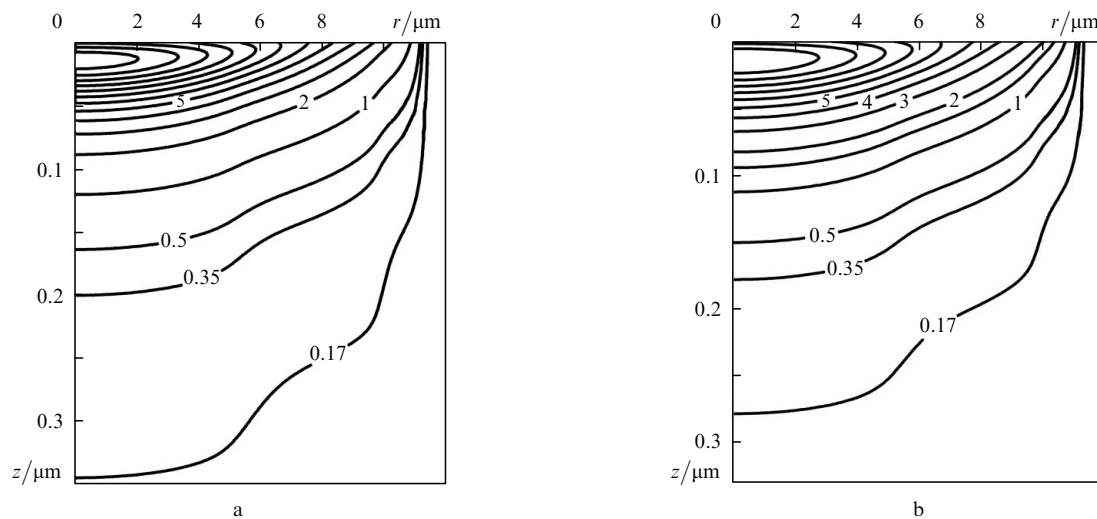
Figure 9. Modelling results for fused silica [66]: isolines of the total energy (in terms of temperature) accumulated in the sample, taking into account the defect energy (a) and defect energy per 1 atom in the sample (b) at the time instant of 3 ps after the maximum of the first pulse. The energy levels are given in eV. The irradiation conditions are the same as in Fig. 8.

the surface (possibly via spinodal decomposition), thus producing a crater whose shape corresponds to the 'critical' temperature isosurface in the sample (~ 0.5 eV for sapphire and 0.35 eV for fused silica, see Fig. 8). One can see from Fig. 8 that the 'critical' isolines are in good qualitative agreement with experimental data on the crater geometry (see insets).

From a thermodynamic point of view we can understand another effect observed in experiments [89], namely, the presence of a convex rim around the edges of the crater on the sapphire surface and its absence on the fused silica surface (see insets in Fig. 8). Although the melting temperature of these materials does not differ too much (2006 K for SiO_2 [98] and 2320 K for Al_2O_3 [93], the extreme isolines in Fig. 8), the processes of their melting are fundamentally different. In sapphire, where melting is a phase transition of the first order, it is accompanied by an abrupt change in material properties: the liquid and solid phases are separated by a fairly sharp melting boundary at which the melting heat is absorbed. In glasses in general, and fused silica in particular, melting is a phase transition of the second order (the melting heat is not spent on this process) which does not suggest drastic changes in material properties (e.g., density or viscosity). Thus, the glass viscosity varies smoothly with heating, while the melt in sapphire has a low viscosity and is sensitive to small perturbations [99]. During spinodal decay, the vapour particles, ejected from the surface, have a high kinetic energy [97], and the recoil pressure of the vapour pushes the low-viscous melt from the crater, forming a rim around it, which quickly solidifies when in contact with a cold solid surface [98, 100]. It is precisely this pattern that is observed on the sapphire surface. In fused silica, where the melt is much more viscous than that in sapphire, the formed recoil pressure, apparently, cannot lead to 'splashing of' the viscous material outside the crater.

Note that a more detailed analysis should take into account additional factors (e.g., surface quality, surface tension, thermal conductivity), which may influence the formation of craters and other microstructures on the material surface. Unfortunately, the behaviour of the thermodynamic parameters of some materials at extreme temperatures is still poorly studied. According to dynamic scaling theory [101], in the ultrafast processes the physical properties of materials have no time to relax to equilibrium values, and therefore we restrict our consideration to the simulation results based on the parameters known from the literature.

4.3 A 'solid' plasma as the cause of shaping

We have shown above that the modulated temperature isosurfaces are formed in fused silica irradiated by trains of laser pulses with a certain time separation between them. What is the real reason for their formation? The answer to this question is provided by Figure 10, which presents the isolines (isosurfaces) of the free electron concentration corresponding to Fig. 8, but for the instant of time before the third laser pulse. In sapphire (Fig. 10a) due to slow recombination of electrons generated by successive pulses, the maximum concentration of free electrons corresponds to the centre of the irradiation spot, resulting in more efficient absorption of laser energy in this region and, accordingly, in greater heating of the material. In general, the isolines of the temperature (Fig. 8a) and free electron concentration (Fig. 10a) for sapphire are similar. In fused silica the pattern of isolines of the electron concentration (see Fig. 10b) is more complicated. Because of a fast trapping of electrons in localised states in the surface layer the electron concentration is lower at the centre of the irradiation spot than at the spot periphery.

Thus, the surface layer of the silica irradiated by a pulse train forms an annular zone with a high concentration of free electrons; the energy of the next pulse is absorbed more efficiently in this zone, while laser radiation penetrates deeper into the sample in its central part. Consequently, the real cause of the spatial modulation of the craters is the formation of a particular spatial density distribution of the free electrons that makes the complex absorption geometry of subsequent laser pulses. We can expect an increase in the number of pulses in the train may form more distinct step-like structures. In Section 5 some conclusions presented here will be used to analyse the processes occurring in the glasses when writing waveguide structures in them.
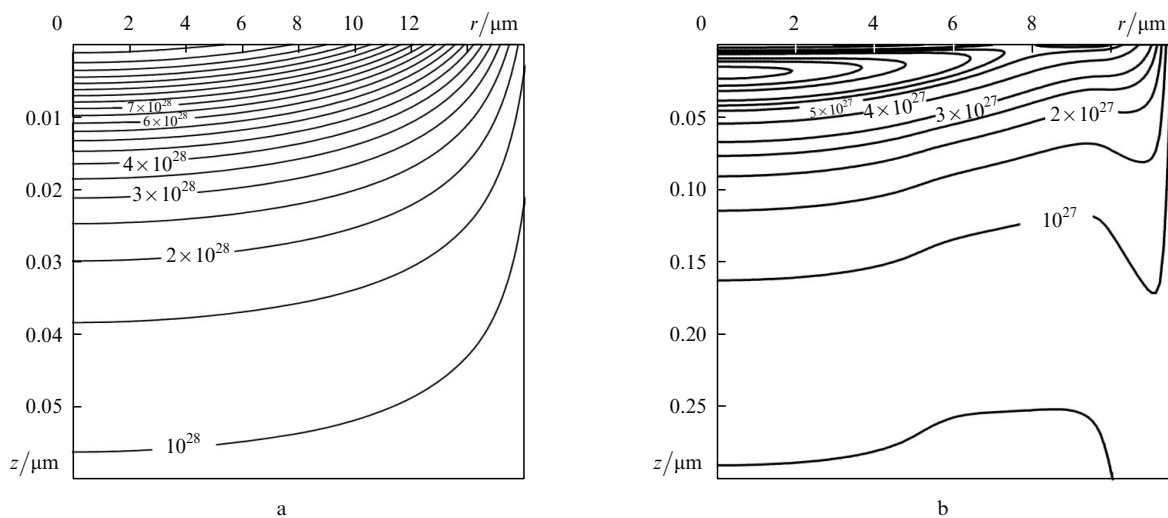

Figure 10. Isolines of the free electron concentration in Al_2O_3 (a) and SiO_2 (b) samples under the same irradiation conditions as in Figs 8 and 9 [66]. The time instant is 1.2 ps after the peak of the first pulse. The concentration is given in m^{-3}.

5. Modelling the formation of waveguide structures in optical glasses

The previous sections presented the basic provisions of the model developed to describe the effect of focusing ultra-short laser pulses on the surface of transparent materials, and described the results of one- and two-dimensional modelling. Irradiation of the surface of transparent materials is widely used for a variety of optical applications, including cleaning, structuring, and modification of surfaces of optical elements. However, of greater interest are the regimes of focusing ultrashort laser pulses inside the transparent crystals and glasses, leading to important for photonics and optoelectronics local modification of the properties of the irradiated sample. The main application field here is the formation of waveguide structures, based on a controlled change in the refractive index in laser-modified regions. Formation of a phase object embedded in the dielectric is caused by the rearrangement of bonds in the sample with the displacement of atoms and a corresponding change in the density, the accumulation of stresses and the appearance of colour centres [14 – 19, 102 – 105]. To control the transformation of the material by pulsed laser radiation and to produce the desired modifications of the optical properties of the material requires a detailed study of both individual laser-induced processes and their relationship from the photoexcitation of the material to obtainment of the spatial optical structure embedded into the matrix of the original material.

The authors of papers [19, 106 – 108] made modelling-based attempts to trace the chain of processes leading to laser-induced transformation of optical material properties, including spatiotemporal dynamics of radiation absorption [19, 106, 107], propagation of elastoplastic waves and plastic deformations caused by them [19, 108], and to identify the role of thermal processes (heat accumulation, melting and solidification of certain regions of the material) [19]. Using an adaptive algorithm to control the laser pulse shape, the authors of [19] managed to select the regimes of high-quality waveguide structure inscription in borosilicate glass (BK6), which, having a high linear expansion coefficient, tends to form extended areas with a reduced refractive index under the action of femtosecond pulses [102, 109]. The developed model allowed one to understand the mechanisms making it possible to force the material to change its natural behaviour, which opens up ways to optimise the writing of waveguide structures in optical materials, depending on their optical, thermodynamic, and mechanical properties. Let us briefly present the basic provisions of the model.

5.1 Nonlinear Schrödinger equation

Propagation of an electromagnetic wave in transparent materials is usually modelled by the nonlinear Schrödinger equation (NSE), which is an asymptotic approximation of Maxwell's equations used to describe the propagation of the wave packet in a nonlinear medium [110]. In the case of plasma formation on the laser beam path, the propagation dynamics of radiation varies self-consistently, and along with the process of the beam self-focusing due to non-linearity, radiation scattering by the plasma formed in the breakdown becomes significant. To simulate such regimes, the NSE is complemented by the terms taking into account radiation losses spent on the plasma generation and the effect of plasma on the permittivity of the medium

[107, 111 – 114]. The study of these processes, i.e., plasma generation with the definition of spatiotemporal dynamics of the laser radiation in optical glass and subsequent thermomechanical response in writing of waveguide structures is the aim of [19, 107]. Numerical simulation is based on the solution of the NSE written in a cylindrically symmetric form:

$$\frac{\partial \bar{\mathscr{E}}}{\partial z} = \frac{i}{2k_0} T^{-1} \left(\frac{\partial^2}{\partial r^2} + \frac{1}{r} \frac{\partial}{\partial r} \right) \bar{\mathscr{E}} - \frac{ik''}{2} \frac{\partial^2 \bar{\mathscr{E}}}{\partial t^2} + \frac{ik_0 n_2 T}{n_0}$$

$$\times \left[(1 - f_R) |\bar{\mathscr{E}}|^2 + f_R \int_{-\infty}^{t} R(t - \tau) |\bar{\mathscr{E}}|^2 d\tau \right] \bar{\mathscr{E}}$$

$$- \frac{\sigma}{2} (1 + i\omega_0 \tau_c) T^{-1} (n_e \bar{\mathscr{E}}) - \frac{1}{2} \frac{W_{mph}(|\bar{\mathscr{E}}|) E_g}{|\bar{\mathscr{E}}|^2} \bar{\mathscr{E}}. \quad (19)$$

Here, $\bar{\mathscr{E}}$ is the complex amplitude of the electric field strength of a light wave. For a Gaussian beam with cylindrical symmetry we have

$$\bar{\mathscr{E}}(r, t, 0) = \bar{\mathscr{E}}_0 \exp \left(-\frac{r^2}{2} - \frac{t^2}{\tau_{las}^2} - \frac{ik_0 r^2}{2f} \right), \quad (20)$$

where $\bar{\mathscr{E}}_0^2 = 2E_{in}/(\pi w^2 \tau_{las} \sqrt{\pi/2})$ is the input beam intensity; $f = (d + z_f^2/d)$ is the radius of curvature of the laser beam at a distance d to the geometric focus with which the calculation begins; z_f is the Rayleigh length; E_{in} is the pulse energy; w is the beam waist; τ_{las} is the pulse duration (half-width determined by a decrease in the field envelope by $1/e$ times); $k_0 = n_0 \omega_0/c$ and ω_0 are the wave number and frequency of the carrier wave; the parameter k'' describes the second-order group velocity dispersion; n_2 is the nonlinear component of refractive index; $E_g = E_{g0} + e^2 \mathscr{E}^2/(2cn_0 \varepsilon_0 m_r \omega_0^2)$ is the effective ionisation potential, taking into account oscillations of the electron energy in the electromagnetic wave; E_{g0} is the dielectric band gap; m_r is the reduced mass of the electron and hole. Equation (19) takes into account the beam diffraction in the transverse direction, group-velocity dispersion, optical Kerr effect with a term corresponding to the delayed (Raman) response of the nonlinear material (characterised by a parameter f_R), plasma defocusing, energy absorption due to photoionisation and inverse bremsstrahlung scattering. The operator $T = 1 + (i/\omega_0) \times (\partial/\partial t)$ describes the self-steepening effects. The inverse bremsstrahlung is described by the Drude theory (see Section 2) with the absorption cross section $\sigma = k_0 e^2 \omega_0 \tau_c \times [n_0^2 \omega_0^2 \varepsilon_0 m_e (1 + \omega_0^2 \tau_c^2)]^{-1}$, where the characteristic time for collisions between electrons τ_c is of the order of a few femtoseconds [115], and we take $\omega_0 \tau_c = 3$.

It should be noted that the linear term in (19) describing the absorption, may slightly underestimate the absorption efficiency when the free electron concentration increases, because the influence of the electron concentration on the absorption cross section is not taken into account. In addition, the influence of multiphoton absorption by free electrons is neglected, which may be important at relatively high radiation intensities [49]; however, by focusing a laser pulse into the target, the clamping effect limits the achievable intensities [32, 33]. The equation describing the formation and recombination kinetics of free electrons is written similarly to (1):

$$\frac{\partial n_{\mathrm{e}}}{\partial t} = \left[W_{\mathrm{mph}}(|\bar{\mathscr{E}}|) + \frac{\sigma n_{\mathrm{e}}}{(1 + m_{\mathrm{r}}/m_{\mathrm{e}})E_{\mathrm{g}}}|\bar{\mathscr{E}}|^2 \right] \frac{n_{\mathrm{a}}}{n_{\mathrm{lat}}} - \frac{n_{\mathrm{e}}}{t_{\mathrm{tr}}}. \quad (21)$$

Thus, equation (21) takes into account the production of free electrons in the multiphoton and collisional ionisation and their annihilation in trapping in the localised states associated with local deformations of the atomic lattice (see Section 2). Here we ignore the effects of heat transfer in the electron system. We assume that after the laser pulse terminates, the locally absorbed time-integrated laser pulse energy ΔE_{L} is transferred to the lattice during the characteristic time of several picoseconds, and the level of the achieved temperature can be estimated as $\Delta E_{\mathrm{L}}/C_{\mathrm{lat}}$. Thus, having a distribution 'map' of the energy absorbed in the sample, we obtain the spatial temperature distribution – the initial data for further modelling of elastic and thermal processes. We emphasise that the processes of radiation absorption, generation and propagation of elastoplastic waves, and heat transfer occur on the pico-, nano- and microsecond time scales, respectively (Fig. 1), which allows us to treat them in stages, simplifying the modelling.

5.2 Effect of the pulse leading edge: absorption localisation, clamping, radiation scattering

At the first stage, equations (19)–(21) are integrated numerically. Figure 11 shows the results of this calculation for fused silica irradiated by pulses from a 800-nm Ti:sapphire laser ($E_{\mathrm{in}} = 1$ μJ, $w = 0.9$ μm, and $\tau_{\mathrm{las}} = 100$ fs) (corresponding to $\tau_{\mathrm{L}} = 120$ fs) [107]. In the calculations, the laser beam is focused at a depth of 90 μm from the sample surface. In simulations we used the following parameters of fused silica: $n_{\mathrm{lat}} = 6.6 \times 10^{22}$ cm^{-3}, $k'' = 361$ fs^2 cm^{-1}, $n_2 = 2.48 \times 10^{-16}$ cm^2 W^{-1}, $E_{\mathrm{g0}} = 9$ eV, $f_{\mathrm{R}} = 0.18$, $m_{\mathrm{r}} = 0.5m_{\mathrm{e}}$, and $t_{\mathrm{tr}} = 150$ fs. The multiphoton ionisation rate was calculated by the Keldysh theory [30]. Figure 11 presents the pulse-integrated spatial distributions of the laser fluence (Fig. 11a) and the energy absorbed by the sample during multiphoton ionisation and inverse bremsstrahlung (Fig. 11b), as well as the distribution of the local peak intensity (Fig. 11c). Due to the fast recombination of free electrons, the distribution of their concentration (Fig. 11d) is given at time 50 fs after the pulse maximum. The inset shows for comparison the experimental image (the same irradiation conditions as in the calculation) obtained by the phase contrast method. When analysing the simulation results the following common features are revealed. The laser radiation energy is absorbed mainly in the region in front of the geometric focus (90 μm). In this area the concentration of free electrons reaches its maximum by the end of the laser pulse. Note that because of fast recombination of electrons, the distribution shown in Fig. 11d differs from that of the earlier stages of the pulse action; however, the electron concentration remains subcritical throughout the irradiation. The white spot on the phase image (see inset) is uniquely associated with the region with the maximum laser energy absorption (~ 60 μm), which leads to the largest thermal expansion of the material. A simple thermodynamic estimate based on the energy absorbed by the electrons ($\Delta E_{\mathrm{L}}/C_{\mathrm{lat}}$) shows that the temperature in the maximum absorption region exceeds the temperature of solidification (glassing). Because of the low thermal conductivity of glasses, this estimate should provide a realistic temperature distribution achieved in the sample

irradiated by femto- and picosecond laser pulses. Note that the energy stored in the defects formed during the electron recombination is not considered here (see Section 4). The boundary of the radiation absorption region in Fig. 11b with the fluence of 1200 J cm^{-2} corresponds to a rise in the sample temperature by about 700 K. The heating in this region contributes to the structural modifications of the glass. By the end of the laser pulse, a channel with a lower density plasma is formed around the focus areas (note that in Fig. 11 the transverse dimension of the calculated structures is presented in a much smaller scale than the longitudinal, in order to show a detailed picture of the laser excitation). The plasma formation leads to 'softening' of molecular matrix and, consequently, to better compaction than in unperturbed regions of glass. It is in this region of softening that flows a highly heated material from the region of maximum excitation. For the regime considered in Fig. 11 the electron energy in the region of maximum absorption is (in accordance with the estimate) ~ 13 eV per electron, which indicates the efficiency of plasma absorption and collisional ionisation.

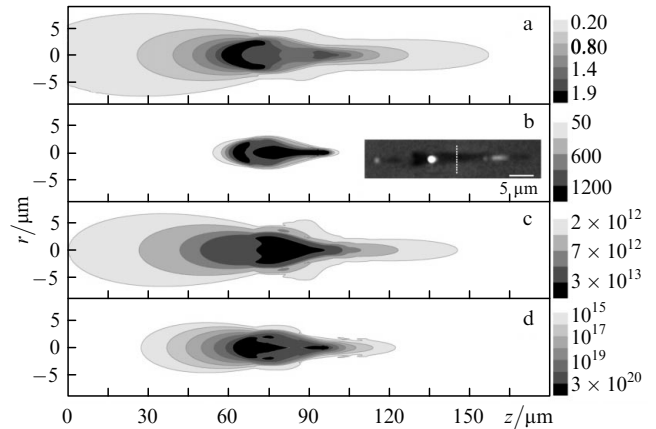**Figure 11.** The simulation results of excitation of a-SiO$_2$ by a Ti:sapphire laser pulse ($\lambda = 800$ nm, $\tau_{\mathrm{L}} = 120$ fs, $E_{\mathrm{in}} = 1$ μJ, $w = 0.9$ μm) [107]: the integral-over-the-pulse fluence distribution (J cm^{-2}) (a) and the energy absorbed in a sample as a result of multiphoton ionisation and inverse bremsstrahlung absorption (J cm^{-3}) (b); distribution of the local peak intensity (W cm^{-2}) (c); the concentration of free electrons at an instant 50 fs after the pulse maximum (cm^{-3}) (d). The inset shows the experimental image of the modified region (irradiation conditions are the same as in the calculations), obtained by the phase contrast method. The geometric focus is shown by a white line.

As seen from the inset in Fig. 11b, we observed in the experiments a significant shift of the generated structures from the point of the geometrical focus towards the laser beam under the experimental conditions. The input radiation power for these conditions (8 MW) exceeds the threshold self-focusing power for fused silica (2.8 MW). Nevertheless, the plasma formation should play the role of a strong defocusing factor which can be seen in Fig. 12. This figure shows the dynamics of laser energy absorption by electrons. To trace which portions of radiation are absorbed most efficiently, the laser pulse of duration 120 fs (FWHM) is divided into four parts and these parts are used to integrate the absorbed energy. It is interesting that only a small fraction of the pulse leading edge, containing about 15% of the pulse energy, is absorbed with maximal

efficiency near and in front of the geometric focus (compare the upper graphs in Figs 12 and 11b). The next part of the laser pulse does not fall into the region near the geometric focus, which is due to strong defocusing scattering of the plasma formed by the pulse leading edge. However, because of self-focusing this part of the pulse creates an absorption maximum at $z = 70$ μm. Thus, the two regions of maximum absorption in Fig. 11b are formed during the first half of the laser pulse, while the second half of the pulse flows around these regions due to the complex correlation of self-focusing and defocusing effects in the region of sharp gradients of the plasma density. An important consequence of this correlation is that the local intensity does not exceed 5×10^{13} W cm^{-2} in the sample (the so-called clamping effect). It is worth noting that radiation attenuation by multiphoton ionisation and inverse bremsstrahlung also plays an important role in the clamping effect [32, 33]. In the context of the clamping effect, the problem of the maximally efficient delivery of the laser energy locally in the sample, which depends on the focusing conditions and more favourable for tight focusing [22], still remains open.
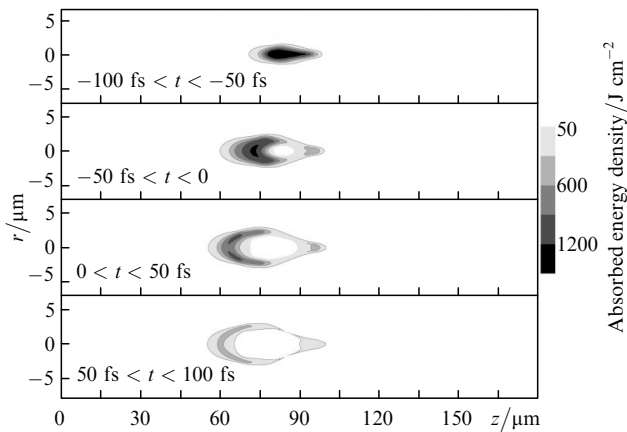

Figure 12. Sequential energy absorption in a-SiO$_2$ for the same irradiation conditions as in Fig. 11 [107]. The pulse maximum corresponds to $t = 0$, the pulse is divided into four time periods to integrate the absorbed energy.

5.3 Elastoplastic deformations and heat dynamics; removal of deformations by fusion

Knowing the distribution of the energy deposited by a femto- or picosecond laser pulse into the sample, one can trace further the evolution of the material. Sharp temperature gradients in the region of radiation absorption lead to generation of elastoplastic waves (or even shock waves, depending on the heating conditions) propagating from the heating region already at picosecond time scales. Typically, at times of a few tens of nanoseconds elastoplastic deformations (if there are any) terminate, whereupon the further evolution of the material is due to the slow cooling of the region heated by the laser. We will show below that the heat propagation may provide an impetus for a new redistribution of the density in the material and even the possibility to launch the secondary compression waves.

To study elastoplastic processes in laser-induced heating of glasses under conditions of writing waveguide structures, a model was developed based on the equations of the theory of elasticity and plasticity and heat conduction equation. As the initial data, use was made of the temperature field obtained by solving the NSE, as described in section 5.1. The details of modelling by the finite element method for a cylindrical geometry of irradiation are given in [116] in a simplified case of thin films, and the complete equations can be found in [117]. As a deformation criterion the von Mises yield criterion was used [116, 118]. Figure 13 presents the results of modelling the effects of radiation from a Ti : sapphire laser ($\lambda = 800$ nm, $E_{in} = 0.5$ μJ, $w = 0.9$ μm) on the BK7 target – a fairly cheap glass that suits well optical applications. However, due to the large linear expansion coefficient, relatively large regions with a low refractive index may form in this material. To write high-quality waveguide structures in this glass, Mermillod-Blondin et al. [19] used an adaptive technique to control the laser pulse shape. The initial laser pulse of duration 150 fs leads to a drastic expansion of the material accompanied by the formation of a thin envelope of compaction around the region with a reduced density. Using the adaptive technique, the authors [19] obtained the optimal laser pulse of duration 4.5 ps; as a result of the pulse action, it is possible to suppress the natural tendency of the material to expand and form well-defined waveguide structures. Images of laser modifications in BK7, obtained by the phase contrast method, are shown in the upper part of Fig. 13 for the short pulse (left) and optimal pulse (right).
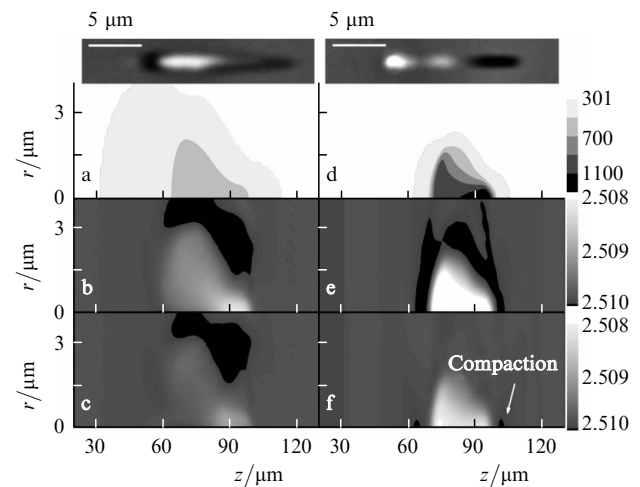

Figure 13. Calculated patterns of heating and plastic deformations in the BK7 glass irradiated by a 150-fs (on the left) and 4.5-ps (on the right) Ti : sapphire laser pulse ($\lambda = 800$ nm, $E_{in} = 0.5$ μJ, $w = 0.9$ μm) [19]: distribution of the absorbed laser energy in temperature units (see the text) (a, d); density distribution (in g cm^{-3}) 10 μs after irradiation (b, e); same as (b, e) 200 μs after irradiation (c, f). At the top of the figure are the experimental images of modifications (irradiation conditions are the same as in calculations, accumulation over 5×10^4 pulses at 100 kHz) obtained by the phase contrast method.

Using the simulations we observed the material evolution during and after irradiation by laser pulses and detected differences that lead to the desired density redistribution in the case of optimal pulses. We identified some key differences between the material response to the short and optimal pulses. For example, the dimensions of the ionisation regions induced by these pulses with initially identical focusing radii are significantly different. The reason lies in the ionisation dynamics. In the case of the short pulse

(similarly to fused silica, see Section 5.2), strong ionisation in front of the geometric focus located at a depth of 90 μm leads (at the beginning of the pulse) to plasma defocusing of the main part of the pulse. As a result of scattering, the laser energy is absorbed by a broader region around the focus than in the case of optimal pulses. In both cases, the density of the produced plasma remains subcritical; however, the maximum electron density is reached in the case of the optimal pulse and by the end of the laser pulse. Obviously, this is probable due to a more effective development of avalanche ionisation in the longer pulses [28, 29]. In addition, at a fixed pulse energy, the self-focusing effects were more pronounced for the short pulse; therefore, the ionisation region in this case is more extended along the beam axis (towards the laser beam). In the case of optimal pulses, the plasma is concentrated near the geometric focus. More importantly, however, that the region of the developed plasma is directly correlated with the region of the effective energy absorption, and hence determines the geometry of the modification developing when a certain threshold energy concentration is achieved. Figure 13 shows the absorbed energy distribution in temperature units for the short and optimal pulses. Interestingly, the fraction of the pulse energy absorbed when irradiating glass, is much greater for short pulses than for optimal pulses ($\sim 65\,\%$ vs. 30 %), but the heating level and degree of its localisation in the case of optimal pulses is much higher. According to the simulations, the maximum temperature reached near the focus in the case of the optimal pulse is ~ 1600 K, i.e., it is 2.5 times higher than when short pulses with the same energy (note that the temperature of BK7 sublimation/evaporation is ~ 2000 K) are used for irradiation.

As noted above, the obtained absorbed energy distributions presented in the form of spatial temperature maps of the sample (Fig. 13a, d), serve as initial data for a thermoelastoplastic model accounting for such effects as the heat transfer, dynamic elasticity, and irreversible deformations of the material. The model assumes that the glass viscosity is large enough so that the material cooling does not result in generation of significant stress waves. Because of these simplifications and absence of information about the temperature dependence of the material properties, the results of this modelling give only a qualitative picture of its behaviour. Based on the modelling, we can give the following general scenario for the development of laser-induced modifications in BK7 under the irradiation conditions considered here. Sharp local heating leads to increased pressure in the heated region, reaching 0.2 GPa for the short pulse and 0.7 GPa for the optimal pulse. The heated material begins to expand, resulting already at picosecond times after pulsed irradiation in the generation of an elastoplastic wave [119]. The wave amplitude depends on the initial temperature gradient and mechanic properties of the material (in particular, on the linear expansion coefficient). The compression wave propagating through the material from the heating region produces plastic deformations in the form of an envelope of compaction around the rarefied region [120]. The region of plastic deformation is determined by the tangential stress when it reaches the material yield stress (~ 7 MPa for VK7). Outside the formed envelope of compaction, the material experiences elastic stress, i.e., the hoop stress is produced. Due to the low thermal conductivity, the heat wave from the hot region achieves the plastic envelope of compaction only

at microsecond times. If the heat level is sufficient to heat the envelope region to the softening temperature, then deformations and hoop stresses are released, accompanied by a new redistribution of the material.

Comparing the modifications induced in BK7 by short and optimal pulses, we recall that the short pulse produces a heated quasi-cylindrical wide region with a temperature not exceeding the softening temperature of glass. Figure 13b shows the material density distribution plotted 10 μs after irradiation by short pulses due to expansion of the heated region and thermoelastoplastic deformations. At a distance of ~ 3 μm from the axis of the structure a more compacted envelope is formed in the deformed material around the rarefied region. At later times, cooling the hot region results only in a slight redistribution of the density. The deformation pattern, formed by the time 200 s (Fig. 13c) is final for the case of irradiation by short pulses. The temperature of the plastic envelope is below the softening temperature of the glass, and therefore in cooling the material the envelope is preserved by preventing the removal of the hoop stress, which remains at a level of 0.8 MPa.

In the case of irradiation by optimal pulses, the density in the heating region is lower due to a greater heating, and the plastic envelope is formed closer to the region of maximum heating, including the end-regions of the structure (Figs 13e, 10 μs after the action of the pulse). The latter is due to significant temperature gradients not only in the radial direction but also along the axis in the focal region. The hoop stress around the region of the plastic deformations is about 3 MPa at this time. When the heat wave from the hot region reaches the plastic envelope, due to strong heating by the optimal pulse the temperature in this region rises above the softening temperature. At this moment, the hoop stress acting on the deformation region pushes the compressed material back into the central rarefied region, thereby leading to a further significant redistribution of the material (cf. Figs 13e and f, which give the final picture of deformations resulting from irradiation by optimal pulses). Although the modelling is performed for single pulses, one can see from Fig. 13f a tendency to an increase in the material density on the structure axis, which is observed experimentally in the case of multipulse irradiation by optimal pulses (Fig. 13, top right).

5.4 Effect of the pulse repetition rate

The question arises how modelling of the single-pulse regime can characterise the real multipulse regimes of inscription of the waveguide structures. It is known that the pulse repetition rate is an important parameter affecting the quality of the index modification. This influence is usually attributed to the effects of the heat accumulation rate [42]. Note that in addition to the effects of heat accumulation, accumulation of deformation states plays an important role. We can assume that by the second irradiation pulse the deformation patterns shown in Fig. 13 have been already formed at a pulse repetition rate of 100 (b, e) and 5 kHz (c, f). Such modelling, when the temperature and density distributions obtained at some time after the pulse were superimposed onto the 'heat map' of the new pulse, showed the following. In the case of irradiation by short pulses, the heat buildup at both repetition rates of 100 and 5 kHz produces no significant qualitative effect on the final structure of deformations, the structure being preserved in the form of a thin envelope of compaction around the

molten region with a gradual accumulation of additional deformations from pulse to pulse, in agreement with the experimental data [19]. However, in the case of irradiation by optimal pulses, the influence of the pulse repetition rate is significant. In this case, modelling the impact of four consecutive pulses separated by 10 and 200 μs showed that at low repetition rates the deformation patterns obtained after irradiation by one or several pulses (cf. Figs 13f and 14b) differ by only a small accumulation of the material in the deformation region from pulse to pulse. However, with increasing the pulse repetition rate we may observe a shift of the material along the axis of the laser beam, whereas the compaction region, which arose after the first laser pulse before the focus in the front region of modification (Fig. 13f), gradually smoothes out and disappears by the fourth pulse (Fig. 14a). In this case, the index growth rate (density in the campaction region) at a high repetition rate is significantly higher, in complete agreement with experimental observations [19].
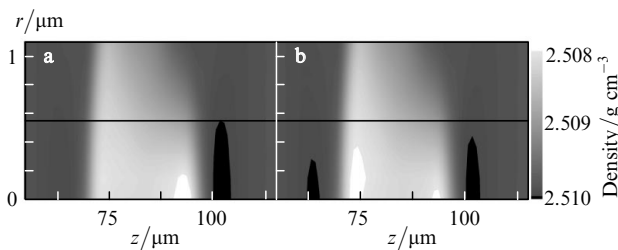

Figure 14. Structure deformations caused by exposure to four consecutive optimal pulses with a repetition rate of 100 (a) and 5 kHz (b) [19]. The irradiation conditions are the same as in Fig. 13. At a higher repetition rate the refractive index grows faster, and the material tends to displace along the laser beam.

6. Conclusions

In this paper we have touched only on some effects that occur both on the surface and in the bulk of the transparent materials irradiated by ultrashort pulses. The developed models (the drift-diffusion approach to the description of effects associated with laser-induced charging of the irradiated surface; the two-dimensional model of the breakdown and heating of dielectrics, developed to study the surface structuring; the combined optical and thermo-elastoplastic approaches to modelling the material modifications in terms of 3D writing of information and waveguide structures) allow us to identify the most important processes that govern the behaviour of the irradiated material versus the laser irradiation conditions. To date, a large amount of impressive experimental data has nevertheless been acquired, which still have not found convincing explanations or adequate descriptions. Here we will mention only some effects.

(i) Formation of micro- and nanovoids inside transparent materials [10, 20–23, 26, 122] is a common effect observed in a variety of transparent crystals and glasses from a certain threshold of the pulse energy [121]. These voids are usually treated as a consequence of a micro-explosion in the local energy release when the pressure can reach 10 TPa [22]. Under certain focusing conditions, chains of voids can appear already in the case of single-pulse

irradiation [122, 123] at sufficiently moderate pulse energies. The question about the level of temperatures reached in the region of the material rupture still remains to be answered because we know from the material science that the material can be destructed at stresses exceeding the limit of its tensile strength, which is usually much smaller than Young's modulus for this material. In addition, with increasing the material temperature (and especially when approaching the melting point and exceeding it) the tensile strength decreases.

(ii) Forming the bulk periodic structures (nanogratings) in transparent materials under the action of linearly polarised ultrashort pulses, first discovered in [9], has resulted in studies of this remarkable phenomenon [10–13, 124–128]. This effect is explained by the interference of incident radiation with the Langmuir waves in the produced plasma [9, 10]. Note that the nanograting period, which is generally much shorter than the irradiation wavelength, decreases with increasing number of laser pulses irradiating a certain amount of material, and with decreasing energy of a single pulse [9]. The nanograting structure produced only in some 'pure' oxide materials (SiO_2, Al_2O_3, TeO_2) consists of alternating regions which are depleted and enriched in oxygen [9]. It remains unclear why nanogratings are not formed in any transparent material (at least in the oxide materials) because the interference should be inherent in any material irradiation. Note that in the case of multipulse irradiation of sapphire, when the sample is shifted (scanned) across the laser beam with a simultaneous shift in its focus toward the sample surface, nanogratings come to the surface without significant changes in the period [124]. The question arises about the relationship of bulk nanogratings and surface periodic structures that emerge under the influence of radiation on various materials (metals, dielectrics, semiconductors) to explain the formation of which some theories have been developed [3–8, 129–131].

(iii) It has been found that when writing waveguide structures with ultrashort pulses in isotropic materials, the writing quality depends on the direction of sample scanning by a laser beam which is associated with a slight laser pulse tilt [132]. At the same time, this effect in the crystals is observed for pulses without a tilt, which is explained by ponderomotive forces acting on the electrons and the resultant heat transfer [133]. However, this phenomenon requires further theoretical and experimental research.

We can mention some other interesting phenomena observed under laser irradiation of transparent materials; for example, changes in the phase state (e.g., laser-induced amorphisation, or, vice versa, crystallisation, formation of nanoclusters of small admixtures, etc.). However, it is clear from the above that the interaction of ultrashort pulses with transparent materials is a phenomenon that is rich in physical content and opens opportunities for its applications in optoelectronics, photonics, and other fields. Attempts to model various processes that accompany this phenomenon are relatively rare, and it is necessary to bend every effort to the theoretical research, which involves pooling the knowledge of optics, solid-state physics and chemistry, plasma physics, thermodynamics, theory of elasticity and plasticity, etc.

References

1. Mao S.S., Quere F., Guizard S., Mao X., Russo R.E., Petite G., Martin P. *Appl. Phys. A*, **79**, 1695 (2004).
2. Gattass R.R., Mazur E. *Nature Photon.*, **2**, 219 (2008).
3. Temple P.A., Soileau M.J. *IEEE J. Quantum Electron.*, **17**, 2067 (1981).
4. Emel'yanov V.I., Konov V.I., Tokarev V.N., Seminogov V.N. *J. Opt. Soc. Am. B*, **6**, 104 (1989).
5. Kerr N.C., Omar B.A., Clark S.E., Emmony D.C. *J. Phys. D*, **23**, 884 (1990).
6. Reif J., Costache F., Henyk M., Pandelov S. *Proc. SPIE Int. Soc. Opt. Eng.*, **4760**, 980 (2002).
7. Dusser B., Sagan Z., Soder H., Faure N., Colombier J.P., Jourlin M., Audouard E. *Opt. Express*, **18**, 2913 (2010).
8. Das S.K., Dasari K., Rosenfeld A., Grunwald R. *Nanotechnology*, **21**, 155302 (2010).
9. Shimotsuma Y., Kazansky P.G., Qiu J.R., Hirao K. *Phys. Rev. Lett.*, **91**, 247405 (2003).
10. Shimotsuma Y., Hirao K., Qiu J.R., Kazansky P.G. *Mod. Phys. Lett. B*, **19**, 225 (2005).
11. Bhardwaj V.R., Simova E., Rajeev P.P., Hnatovsky C., Taylor R.S., Rayner D.M., Corkum P.B. *Phys. Rev. Lett.*, **96**, 057404 (2006).
12. Kazansky P.G., Yang W.J., Bricchi E., Bovatsek J., Arai A., Shimotsuma Y., Miura K., Hirao K. *Appl. Phys. Lett.*, **90**, 151120 (2007).
13. Taylor R.S., Hnatovsky C., Simova E., Rajeev P.P., Rayner D.M., Corkum P.B. *Opt. Lett.*, **32**, 2888 (2007).
14. Hirao K. *Ceram. Jpn.*, **30**, 689 (1995).
15. Miura K., Qiu J., Inouye H., Mitsuyu T., Hirao K. *Appl. Phys. Lett.*, **71**, 3329 (1997).
16. Schaffer C.B., Brodeur A., Garcia J.F., Mazur E. *Opt. Lett.*, **26**, 93 (2001).
17. Wang Z., Sugioka K., Hanada Y., Midorikawa K. *Appl. Phys. A*, **88**, 699 (2007).
18. Yang W., Corbari C., Kazansky P.G., Sakaguchi K., Carvalho I.C.S. *Opt. Express*, **16**, 16215 (2008).
19. Mermillod-Blondin A., Burakov I.M., Meshcheryakov Y.P., Bulgakova N.M., Audouard E., Rosenfeld A., Husakou A., Hertel I.V., Stoian R. *Phys. Rev. B*, **77**, 104205 (2008).
20. Glezer E.N., Mazur E. *Appl. Phys. Lett.*, **71**, 882 (1997).
21. Watanabe W., Itoh K. *Opt. Express*, **10**, 14 (2002).
22. Juodkazis S., Nishimura K., Tanaka S., Misawa H., Gamaly E.G., Luther-Davies B., Hallo L., Nicolai P., Tikhonchuk V.T. *Phys. Rev. Lett.*, **96**, 166101 (2006).
23. Graf R., Frnandez A., Dubov M., Brueckner H.J., Chichkov B.N., Apolonski A. *Appl. Phys. A*, **87**, 21 (2007).
24. Koubassov V., Laprise J.-F., Theberge F., Forster E., Sauerbrey R., Muller B., Glatzel U., Chin S.L. *Appl. Phys. A*, **79**, 499 (2004).
25. Qiu J., Miura K., Hirao K. *J. Non-Cryst. Sol.*, **354**, 1100 (2008).
26. Sugioka K., Hanada Y., Midorikawa K. *Laser Photon. Rev.*, **4**, 386 (2010).
27. Arnold D., Cartier E. *Phys. Rev. B*, **46**, 15102 (1992).
28. Stuart B.C., Feit M.D., Rubenchik A.M., Shore B.W., Perry M.D. *Phys. Rev. Lett.*, **74**, 2248 (1995).
29. Stuart B.C., Feit M.D., Herman S., Rubenchik A.M., Shore B.W., Perry M.D. *Phys. Rev. B*, **53**, 1749 (1996).
30. Keldysh L.V. *Zh. Eksp. Teor. Fiz.*, **47**, 1946 (1964).
31. Kaiser A., Rethfeld B., Vicanek M., Simon G. *Phys. Rev. B*, **61**, 11437 (2000).
32. Becker A., Akozbek N., Vijayalakshmi K., Oral E., Bowden C.M., Chin S.L. *Appl. Phys. B*, **73**, 287 (2001).
33. Sun Q., Liang F., Vallee R., Chin S.L. *Opt. Lett.*, **33**, 2713 (2008).
34. Lenzner M., Krüger J., Sartania S., Cheng Z., Spielmann C., Mourou G., Kautek W., Krausz F. *Phys. Rev. Lett.*, **80**, 4076 (1998).
35. Petrov G.M., Davis J. *J. Phys. B*, **41**, 025601 (2008).
36. Quéré F., Guizard S., Martin P. *Europhys. Lett.*, **56**, 138 (2001).
37. Rajeev P.P., Gertsvolf M., Corcum P.B., Rayner D.M. *Phys. Rev. Lett.*, **102**, 083001 (2009).
38. Jones S.C., Braunlich P., Casper R.T., Shen X.-A., Kelly P. *Opt. Engineer.*, **28**, 1039 (1989).
39. Tanimura K., Fujiwara H., Suzuki T. *Nucl. Instrum. Meth. B*, **116**, 26 (1996).
40. Kruger J., Lenzner M., Martin S., Lenner M., Spielman C., Fiedler A., Kautek W. *Appl. Surf. Sci.*, **208**, 233 (2003).
41. Martin P., Guizard S., Daguzan Ph., Petite G., D'Oliveira P., Maynadier P., Pedrix M. *Phys. Rev. B*, **55**, 5799 (1997).
42. Eaton S.M., Zhang H., Herman P.R., Yoshino F., Shah L., Bovatsek J., Arai A.Y. *Opt. Express*, **13**, 4708 (2005).
43. Stoian R., Rosenfeld A., Ashkenasi D., Hertel I.V., Bulgakova N.M., Campbell E.E.B. *Phys. Rev. Lett.*, **88**, 097603 (2002).
44. Bulgakova N.M., Stoian R., Rosenfeld A., Hertel I.V., Campbell E.E.B. *Phys. Rev. B*, **69**, 054102 (2004).
45. Bulgakova N.M., Stoian R., Rosenfeld A., Hertel I.V., Marine W., Campbell E.E.B. *Appl. Phys. A*, **81**, 345 (2005).
46. Bulgakova N.M., Rosenfeld A., Erentraut L., Stoian R., Hertel I.V. *Proc. SPIE Int. Soc. Opt. Am.*, **6732**, 673208 (2007).
47. Gruzdev V.E. *Phys. Rev. B*, **75**, 205106 (2007).
48. Rethfeld B. *Phys. Rev. Lett.*, **92**, 187401 (2004).
49. Bachau H., Belsky A.N., Bogatyrev I.B., Gaudin J., Geoffroy G., Guizard S., Martin P., Popov Y.V., Vasil'ev A.N., Yatsenko B.N. *Appl. Phys. A*, **98**, 679 (2010).
50. Mishima K., Hayashi M., Yi J., Lin S.H., Selzle H.L., Schlag E.W. *Phys. Rev. A*, **66**, 033401 (2002).
51. Sokolowski-Tinten K., von der Linde D. *Phys. Rev. B*, **61**, 2643 (2000).
52. Driscoll W.G., Vaughan W. (Eds). *Handbook of Optics* (New York: McGraw-Hill Book Company, 1978).
53. Von der Linde D., Schuller H. *J. Opt. Soc. Am. B*, **13**, 216 (1996).
54. Gamaly E.G., Rode A.V., Luther-Davies B., Tikhonchuk V.T. *Phys. Plasmas*, **9**, 949 (2002).
55. Bulgakova N.M., Bulgakov A.V., Zhukov V.P., Marine W., Vorobyev A.Y., Guo C.L. *Proc. SPIE Int. Soc. Opt. Am.*, **7005**, 70050C (2008).
56. Stoian R., Ashkenasi D., Rosenfeld A., Campbell E.E.B. *Phys. Rev. B*, **62**, 13167 (2000).
57. Bashir S., Rafique M.S., Husinsky W. *Appl. Surf. Sci.*, **255**, 8372 (2009).
58. Jones S.C., Fischer A.H., Braunlich P., Kelly P. *Phys. Rev. B*, **37**, 755 (1988).
59. Siekhaus W.J., Kinney J.H., Milam D., Chase L.L. *Appl. Phys. A*, **39**, 163 (1986).
60. Kaganov M.I., Lifshits I.M., Tanatarov L.V. *Zh. Eksp. Teor. Fiz.*, **31**, 232 (1956).
61. Anisimov S.I., Kapeliovich B.L., Perel'man T.L. *Zh. Eksp. Teor. Fiz.*, **66**, 776 (1974).
62. Ivanov D.S., Zhigilei L.V. *Phys. Rev. Lett.*, **98**, 195701 (2007).
63. Ernstorfer R., Harb M., Hebeisen C.T., Sciaini G., Dartigalongue T., Miller R.J.D. *Science*, **323**, 1033 (2009).

64. Van Driel H.M. *Phys. Rev. B*, **35**, 8166 (1987).
65. Bulgakova N.M., Burakov I.M., Meshcheryakov Yu.P., Stoian R., Rosenfeld A., Hertel I.V. *J. Laser Micro/Nanoeng.*, **2**, 76 (2007).
66. Burakov I.M., Bulgakova N.M., Stoian R., Rosenfeld A., Hertel I.V. *Appl. Phys. A*, **81**, 1639 (2005).
67. Tam A.C., Brand J.L., Cheng D.C., Zapka W. *Appl. Phys. Lett.*, **55**, 2045 (1989).
68. Ashkenasi D., Rosenfeld A., Varel H., Warmer M., Campbell E.E.B. *Appl. Surf. Sci.*, **120**, 65 (1997).
69. Varel H., Wahmer M., Rosenfeld A., Ashkenasi D., Campbell E.E.B. *Appl. Surf. Sci.*, **127-129**, 128 (1998).
70. Stoian R., Ashkenasi D., Rosenfeld A., Wittmann M., Kelly R., Campbell E.E.B. *Nucl. Instrum. Methods Phys. Res. B*, **166-167**, 682 (2000).
71. Kelly R., Miotello A. *Nucl. Instrum. Methods Phys. Res. B*, **122**, 374 (1997).
72. Bulgakova N.M., Bulgakov A.V. *Appl. Phys. A*, **73**, 199 (2001).
73. Henyk M., Wolfframm D., Reif J. *Appl. Surf Sci.*, **168**, 263 (2000).
74. Bulgakova N.M., Bulgakov A.V., Bobrenok O.F. *Phys. Rev. E*, **62**, 5624 (2000).
75. Stoian R., Rosenfeld A., Hertel I.V., Bulgakova N.M., Campbell E.E.B. *Appl. Phys. Lett.*, **85**, 694 (2004).
76. Borghesi M., Romagnani L., Schiavi A., Campbell D.H., Haines M.G., Willi O., Mackinnon A.J., Galimberti M., Gizzi L., Clarke R.J., Hawkes S. *Appl. Phys. Lett.*, **82**, 1529 (2003).
77. Vella A., Deconihout B., Marucci L., Santamato E. *Phys. Rev. Lett.*, **99**, 046103 (2007).
78. Marine W., Bulgakova N.M., Patrone L., Ozerov I. *Appl. Phys. A*, **79**, 771 (2004).
79. Marine W., Bulgakova N.M., Patrone L., Ozerov I. *J. Appl. Phys.*, **103**, 094902 (2008).
80. Li M., Menon S., Nibarger J.P., Gibson G.N. *Phys. Rev. Lett.*, **82**, 2394 (1999).
81. Hughes R.C. *Phys. Rev. B*, **19**, 5318 (1979).
82. Miotello A., Dapor M. *Phys. Rev. B*, **56**, 2241 (1997).
83. Riffe D.M., Wang X.Y., Downer M.C., Fisher D.L., Tajima T., Erskine J.L., More R.M. *J. Opt. Soc. Am. B*, **10**, 1424 (1993).
84. Zhigilei L.V. *Appl. Phys. A*, **76**, 339 (2003).
85. Meshulach D., Silberberg Y. *Nature*, **396**, 239 (1998).
86. Assion A., Baumert T., Bergt M., Brixner T., Kiefer B., Seyfried V., Strehle M., Gerber G. *Science*, **282**, 919 (1998).
87. Glinka Y.D., Lin S.-H., Hwang L.-P., Chen Y.-T., Tolk N.H. *Phys. Rev. B*, **64**, 085421 (2001).
88. Stoian R., Boyle M., Thoss A., Rosenfeld A., Korn G., Hertel I.V., Campbell E.E.B. *Appl. Phys. Lett.*, **80**, 353 (2002).
89. Stoian R., Boyle M., Thoss A., Rosenfeld A., Korn G., Hertel I.V. *Appl. Phys. A*, **77**, 265 (2003).
90. Guizard S., Semerok A., Gaudin J., Hashida M., Martin P., Qutéré F. *Appl. Surf. Sci.*, **186**, 364 (2002).
91. Jiang L., Tsai H.L. *J. Phys. D: Appl. Phys.*, **37**, 1492 (2004).
92. Bulgakova N.M., Stoian R., Rosenfeld A., Marine W., Campbell E.E.B. *Proc. SPIE Int. Soc. Opt. Eng.*, **5448**, 121 (2004).
93. Grigor'ev I.S., Meilikhov E.Z. (Eds) *Handbook of Physical Quantities* (Boca Raton, FL: CRC Press, 1997; Moscow: Energoatomizdat, 1991).
94. Skripov V.P. *Metastable Liquids* (New York: Wiley, 1974; Moscow: Nauka, 1972).
95. Bulgakova N.M., Bourakov I.M. *Appl. Surf. Sci.*, **197-198**, 41 (2002).
96. Zel'dovich Ya.B., Todes O.M. *Zh. Eksp. Teor. Fiz.*, **10**, 1441 (1940).
97. Martynyuk M.M., Kravchenko N.Yu. *Prikl. Fiz.*, **1**, 79 (2003).
98. Siegel J., Ettrich K., Welsch E., Matthias E. *Appl. Phys. A*, **64**, 213 (1997).
99. Nubling R.K., Harrington J.A. *Appl. Opt.*, **36**, 5934 (1997).
100. Korner C., Mayerhofer R., Hartmann M., Bergmann H.W. *Appl. Phys. A*, **63**, 123 (1996).
101. Anisimov M.A. *Critical Phenomena in Liquids and Liquid Crystals* (Philadelphia: Gordon and Breach, 1991; Moscow: Nauka, 1987).
102. Bhardwaj V.R., Simova E., Corkum P.B., Rayner D.M., Hnatovsky C., Taylor R.S., Schreder B., Kluge M., Zimmer J. *J. Appl. Phys.*, **97**, 083102 (2005).
103. Osellame R., Chiodo N., Maselli V., Yin A., Zavelani-Rossi M., Cerullo G., Laporta P., Aiello L., De Nicola S., Ferraro P., Finizio A., Pierattini G. *Opt. Express*, **13**, 612 (2005).
104. Chan J.W., Huser T.R., Risbud S.H., Hayden J.S., Krol D.M. *Appl. Phys. Lett.*, **82**, 2371 (2003).
105. Daguzan P., Martin P., Guizard S., Petite G. *Phys. Rev. B*, **52**, 17099 (1995).
106. Winkler S.W., Burakov I.M., Stoian R., Bulgakova N.M., Husakou A., Mermillod-Blondin A., Rosenfeld A., Ashkenasi D., Hertel I.V. *Appl. Phys. A*, **84**, 413 (2006).
107. Burakov I.M., Bulgakova N.M., Stoian R., Mermillod-Blondin A., Audouard E., Rosenfeld A., Husakou A., Hertel I.V. *J. Appl. Phys.*, **101**, 043506 (2007).
108. Mermillod-Blondin A., Bonse J., Rosenfeld A., Hertel I.V., Meshcheryakov Y.P., Bulgakova N.M., Audouard E., Stoian R. *Appl. Phys. Lett.*, **94**, 041911 (2009).
109. Ehrt D., Kittel T., Will M., Nolte S., Tünnermann A. *J. Non-Cryst. Sol.*, **345-346**, 332 (2004).
110. Temam R., Miranville A. *Mathematical Modeling in Continuum Mechanics* (Cambridge: Cambridge University Press, 2005).
111. Gaeta A.L. *Phys. Rev. Lett.*, **84**, 3582 (2000).
112. Couairon A., Sudrie L., Franco M., Prade B., Mysyrowicz A. *Phys. Rev. B*, **71**, 125435 (2005).
113. Couairon A., Mysyrowicz A. *Phys. Rep.*, **441**, 47 (2007).
114. Kandidov V.P., Shlenov S.A., Kosareva O.G. *Kvantovaya Elektron.*, **39**, 205 (2009) [*Quantum Electron.*, **39**, 205 (2009)].
115. Sun Q., Jiang H., Liu Y., Wu Z., Yang H., Gong Q. *Opt. Lett.*, **30**, 320 (2005).
116. Meshcheryakov Y.P., Bulgakova N.M. *Appl. Phys. A*, **82**, 363 (2006).
117. Timoshenko S.P., Goodier J.N. *Theory of Elasticity* (New-York: McGraw-Hill, 1970).
118. Wilkins M.L., in *Methods in Computational Physics, Fundamental Methods in Hydrodynamics* (New York: Acad. Press, 1964) Vol. 3, p. 211.
119. Sakakura M., Terazima M., Shimotsuma Y., Miura K., Hirao K. *Opt. Express*, **15**, 5674 (2007).
120. Hallo L., Bourgeade A., Tikhonchuk V.T., Mezel C., Breil J. *Phys. Rev. B*, **76**, 024101 (2007).
121. Hashimoto T., Juodkazis S., Misawa H. *New J. Phys.*, **9**, 253 (2007).
122. Sun H., Song J., Li C., Xu J., Wang X., Cheng Y., Xu Z., Qiu J., Jia T. *Appl. Phys. A*, **88**, 285 (2007).
123. Beresna M., Bulgakova N.M., Kazansky P.G. *Submitted*.
124. Hörstmann-Jungemann M., Gottmann J., Wortmann D.J. *J. Laser Micro/Nanoeng.*, **4**, 135 (2009).
125. Cheng G., Mishchik K., Mauclair C., Audouard E., Stoian R. *Opt. Exp.*, **17**, 9515 (2009).

126. Liang F., Sun Q., Gingras D., Vallée R., Chin S.L. *Appl. Phys. Lett.*, **96**, 101903 (2010).
127. Ramirez L.P.R., Heinrich M., Richter S., Dreisow F., Keil R., Korovin A.V., Peschel U., Nolte S., Tunnermann A. *Appl. Phys. A*, **100**, 1 (2010).
128. Beresna M., Kazansky P.G. *Opt. Lett.*, **35**, 1662 (2010).
129. Van Driel H.M., Sipe J.E., Young J.F. *Phys. Rev. Lett.*, **49**, 1955 (1982).
130. Dufft D., Rosenfeld A., Das S.K., Grunwald R., Bonse J. *J. Appl. Phys.*, **105**, 034908 (2009).
131. Golosov E.V., Emel'yanov V.I., Ionin A.A., Kolobov Yu.P., Kudryashov S.I., Ligachev A.E., Novoselov Yu.N., Seleznev L.V., Sinitsyn D.V. *Pis'ma Zh. Eksp. Teor. Fiz.*, **90**, 116 (2009).
132. Yang W., Kazansky P.G., Shimotsuma Y., Sakakura M., Miura K., Hirao K. *Appl. Phys. Lett.*, **93**, 171109 (2008).
133. Yang W., Kazansky P.G., Svirko Y.P. *Nat. Photon.*, **2**, 99 (2008).